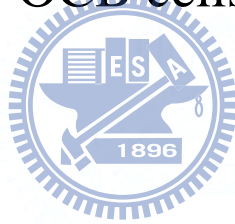


國立交通大學

顯示科技研究所

碩士論文

表面奈米結構於 OCB cells 內成核現象之研究



The study of surface nanostructure nucleation process in
OCB cells

研究生：張毓筠

指導教授：陳皇銘

中華民國九十八年七月

表面奈米結構於 OCB cells 內成核現象之研究

The study of surface nanostructure nucleation process in OCB cells

研究生：張毓筠

Student : Yu-Yun Chang

指導教授：陳皇銘

Advisor : Huang-Ming Philip Chen

國立交通大學
電機學院
顯示科技研究所
碩士論文



Submitted to Display Institute

College of Electrical Engineering

National Chiao Tung University

in Partial Fulfillment of the Requirements

for the Degree of

Master

In

Display Institute

July 2009

Hsinchu, Taiwan, Republic of China.

中華民國九十八年七月

表面奈米結構於 OCB cells 內成核現象之研究

研究生：張毓筠

指導教授：陳皇銘 博士

國立交通大學顯示科技所

摘要

近年來，TFT LCD-TVs 在數位電視的市場需求急驟增加，因為液晶顯示器擁有高解析度、低損耗能量以及輕薄短小的外型，使的傳統的 CRT 漸漸被液晶顯示器所取代。然而在液晶顯示器的應用上，依然存在著一些問題，例如在動畫時產生的畫面模糊或殘影問題，此現象在大尺寸及 3D 顯示器上容易發生。然而造成此現象的主要原因為液晶反應速度不夠快。



光學補償彎曲液晶盒(optically compensated bend ,OCB 或稱 Pi-cell)以擁有快速反應速度及廣視角而聞名，因此近年來更為許多團體主要的研究對象。然而此模態的液晶盒存在著視角以及必須預先轉態的問題，在許多其他的研究中曾成功的降低轉態的時間，但卻會造成原本光學特性的喪失，例如對比度下降，或需要一個較高的脈衝電壓來完成瞬間的轉態，然而此方法無法用在一般的 TFT 驅動電路上。

在本論文中，提出一新穎的方法，在導電玻璃表面製作奈米突起，使光學補償彎曲液晶盒在不需高電壓的驅動下加速成核現象，達到快速的轉態，並保留此液晶盒的原本光學特性。

The study of surface nanostructure nucleation process in OCB cells

Student: Yu-Yun Chang

Advisor: Dr. Huang-Ming Philip Chen

**Display Institute
National Chiao Tung University**

Abstract

Recently, the needs for TFT LCD-TVs have dramatically increased by the expansion of the digital-TV market. LCD-TVs have lots of advantages of high resolution, low power consumption, light weight, slim size and so on. However, they have some drawbacks for TV application, especially motion image blur which results from slow response time. Motion image blur is recognized easily for a large screen and 3D LCD-TVs. Optically Compensated Bend (OCB) mode LCD, which has the characteristics of fast response and wide viewing angle becomes a new target to the researchers.

Nevertheless, there are some drawbacks of OCB cell, for example, low contrast ratio and pre-transition. Techniques for fast splay to bend transition have received increasingly attention. Although some techniques successfully induced bend transition, most of the techniques sacrificed contrast ratio of the devices or needed a high pulse voltage to form the fast transition. The high voltage ($>10V$) is not suitable for TFT devices.

In this thesis, we present a novel method to form bend transition cores which can spread uniformly in each pixel without applying the high pulse voltage and losing of optic efficiency.

誌謝

在碩士兩年的學習當中，雖然多次因實驗遇到困境而沮喪，但有了許多人的幫助與陪伴，最後終於順利完成。特別感謝我的指導教授陳皇銘老師，不論在生活上、課業上，都給予了很大的幫助，給予我們一個廣闊的視野，時時提醒我們做研究的態度，讓我在碩士兩年之中獲益良多。

感謝實驗室的學長姊們，蓮馨、洪文、祥志、謹璋、怡帆、宜揚的教導，讓我可以更快的熟悉整個實驗室，並在我的研究中適時提出建議。感謝我的同學們，致弋、承富、宣穎，這兩年來一起互相勉勵走過。特別感謝學弟厚茨，幫我分擔實驗上的工作量，也感謝實驗室的其他學弟妹們，總是為實驗室帶來很多歡樂。

感謝佩宜和永星，實驗室及無塵室有了你們的照顧，讓生活以及實驗品質有了更佳的改善。特別感謝其他實驗室的學長姊以及同學們，司芬、阿寬、上傑、冠霖、浩志、樂咖、凱凱、阿達、DADSLab 的成員們……等，教導我使用機台，並在生活上給予我莫大的幫助。

特別感謝我的大學同學，國佩、怡菁、享穎、伶郁、奕碩、詩鎰、士豪、孟珊，總是在我最無助的時候，給我最溫暖的懷抱，感謝你們的陪伴，讓我順利走到這裡。

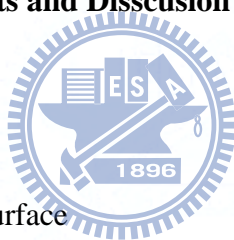
最後，感謝我的家人，總是給予我最大的支持，讓我順利的完成學業。

Table of contents

Abstract in Chinese	i
Abstract in English	ii
Acknowledgement	iii
Table of contents	iv
List of Tables	vi
List of Figures	vii
Chapter 1 Introduction	1
1.1 Introduction of Liquid Crystal	1
1.2 Liquid Crystal Phase	1
1.2.1 Nematic	3
1.2.2 Smectic	3
1.2.3 Cholesteric	4
1.3 Liquid Crystal Optics	4
1.3.1 The Basic Properties of Light	5
1.3.2 Light Waves Propagation in Uniaxial Medium	6
1.4 Operation Method of LCD	8
1.5 Optical Compensated Bend Mode (OCB)	9
1.6 Motivation and Objective	10
1.7 Organization of This Thesis	10
Chapter 2 Overview of OCB Cell	11
2.1 Characteristics of OCB Cell	11
2.1.1 OCB Cell Structure	11
2.1.2 Wide Viewing Angle	12
2.1.3 Fast Response Time	13
2.1.4 Phase Transition Mechanism	14



2.2	Nucleation	16
2.2.1	Nucleation Theory	16
2.2.2	Nucleation Rate	20
2.2.3	Review the Study of Nucleation in OCB cell	21
2.3	Summary	26
Chapter 3 Measurement Systems		27
3.1	Introduction	27
3.2	Atomic Force Microscope (AFM)	27
3.3	Cell Gap Measurement System	30
3.4	Polarizing Optical Microscope (POM)	33
3.5	Laser Optics System	35
Chapter 4 Experimental Results and Discussion		36
4.1	Introduction	36
4.2	Cell Fabrication Process	38
4.3	Optimum Nanostructure Surface	43
4.3.1	Nano-particle in DI water	43
4.3.2	Nano-particle in PVA Solution	45
4.3.3	Nano-particle in EG and PGMEA Mixed Solution	48
4.3.4	Summary	52
4.4	Transition Time Measurement	52
4.5	Measurement of Electro-Optical Properties	55
4.6	Discussion	56
Chapter 5 Conclusions		61
5.1	Conclusions	61
5.2	Future work	61
References		63



List of Tables

Table 4-1	Parameters of spin coating nanoparticle	39
Table 4-2	Parameters of spin coating mixture solution.....	39
Table 4-3	Parameters of spin coating mixture solution.....	40
Table 4-4	Parameters of spin coating polyimide.....	41
Table 4-5	Rubbing Conditions for Polyimide glasses.....	41
Table 4-6	The specification of liquid crystal material ZCE-5096XX.....	42
Table 4-7	Comparison of transition time with PVA and PI alignment.....	47
Table 4-8	The transition time during nucleation for 90nm nano-particle (cell gap~4.67 μ m).	54
Table 4-9	The transition time during nucleation for 90nm nano-particle (cell gap~2.8 μ m).	54
Table 4-10	The transition time during nucleation for 50 nm nano-particle (cell gap~4.67 μ m).	55
Table 4-11	The transition time during nucleation for 50 nm nano-particle (cell gap~2.8 μ m).	55



List of Figures

Fig. 1-1	Types of rod-like liquid crystals. (a) Nematic liquid crystal. (b) Smectic liquid crystal (A type). (c) Cholesteric liquid crystal.....	2
Fig. 2-1	The structure of the π cell.	12
Fig. 2-2	Experimental results of the viewing angle dependent transmittance for TN cell and OCB cell.....	13
Fig. 2-3	Cross-section view of OCB cell.	13
Fig. 2-4	(a) splay state, (b) Vcr, bend mode, and OCB cell is in the bright state. (c) Von, homeotropic state, and OCB cell is in the dark state.....	14
Fig. 2-5	Schematic figure of the dynamics in the π cell. The flow induces the torque to accelerate to relax.	14
Fig. 2-6	Five configurations of pi-cell. Dotted lines indicate nucleation processes.	15
Fig. 2-7	The activation energy barrier ΔG^* and the critical nucleus size r^* according to classical nucleation theory based on heterophase fluctuations.....	18
Fig. 2-8	Difference in energy barriers of homogeneous and heterogeneous nucleation. ..	19
Fig. 2-9	Mechanism of bend transition.	21
Fig. 2-10	Order parameter profile of simulation.	22
Fig. 2-11	(a) Microscopic image of DDB cell. (b) Schematic diagram of the director profile of each domain. (c) Cross-sectional structure of DDB cell.....	24
Fig. 2-12	Free energy of the bend and splay configurations vs. applied voltage in the pi-cells.....	25
Fig. 2-13	The scheme of high tilt angle alignment cell.....	25
Fig. 2-14	Schematic diagram of polymer wall.....	26
Fig. 3-1	Concept of AFM and the optical lever.	28
Fig. 3-2	The picture of LAMBDA 650 PerKin Elmer.	31
Fig. 3-3	Two reflecting surfaces separated by a layer causing light interference. The dotted line indicates the first internal reflection.	32
Fig. 3-4	Example of cell gap measurement.	33
Fig. 3-5	The picture of POM Olympus BX51.....	34
Fig. 3-6	Schematic of the laser optics system.	35
Fig. 4-1	The diagram of mixed method.....	37

Fig. 4-2	The flowchart of cell fabrication process.	38
Fig. 4-3	Schematic illustration of nanostructured surface.....	43
Fig. 4-4	The AFM images of different concentration.	44
Fig. 4-5	The relation between concentration (wt%) and distribution density (μm^{-2}).....	44
Fig. 4-6	Schematic illustration of nanostructured surface.....	45
Fig. 4-7	The AFM images of different concentration.	46
Fig. 4-8	The relation between concentration (wt%) and distribution density (μm^{-2}).....	47
Fig. 4-9	Schematic illustration of nanostructured surface.....	48
Fig. 4-10	The AFM images of 90nm nano-particle at different concentration. (a) Around the center of ITO surface. (b) Around the edge of ITO surface.....	49
Fig. 4-11	The AFM images of 50nm nano-particle at different concentration. (a) Around the center of ITO surface. (b) Around the edge of ITO surface.....	50
Fig. 4-12	The relation between concentration (wt%) and protrusion volume distribution density (nm^3/nm^2). The solid line is the calculated trend line.	52
Fig. 4-13	Picture of nucleation process of (A) conventional Pi-cell and (B) nanostructure treated cell. The (a)(b)(c)(d) are the splay state, Ha to bend state, bend state, and twist to splay state, respectively.....	53
Fig. 4-14	The V-T curves in difference nano-particle concentration.	56
Fig. 4-15	The trend of transition time (sec) regarding to the protrusion volume density (nm^3/nm^2). (a) Applied 6V. (b) When applied voltage around critical voltage. The solid line indicates the exponential trend line.	58

Chapter 1

Introduction

1.1 Introduction of Liquid Crystal

Liquid crystalline phase was first discovered by Dr. F. Reiner [1] in 1888 and the well known term “liquid crystal” was introduced by Lehmann [2] in 1890. Liquid crystals are substances that exhibit a phase of matter that has properties between those of an isotropic liquid, and those of a solid crystal. There are many different types of liquid crystal phases, also called “mesophases”, which can be distinguished based on their different optical properties.

Because LC displays have many advantages, such as thin, light weight, low power consumption, no radiation pollution, and the most important, compatible with semi-conductor technology. The LC displays become the lead of planar display market.

1.2 Liquid Crystal Phase

Liquid crystal phase is a state between solid state and liquid state, also called the forth state or mesophase. As a result, it has both the solid character and liquid characters. Liquid crystal phases are classified by several configurations of molecules which widely differ in their structure. The structures of LC molecules are asymmetric, can be classified into two

major shapes, rod-like and disk-like. Generally, rod-like molecules tend to orient themselves around the rubbing direction and align parallel to each other to a preferred direction which is so called self-assembly. Rod-like liquid crystal material can be divided into three major types of liquid crystals—Nematic, Smectic, and Cholesteric.(Fig. 1-1)

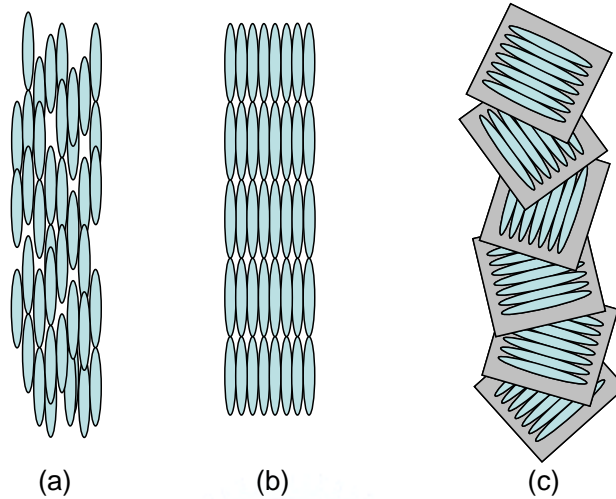
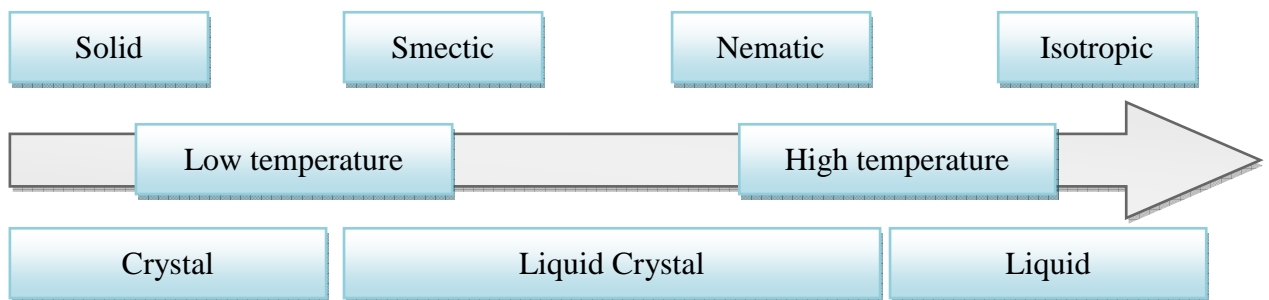


Fig. 1-1 Types of rod-like liquid crystals. (a) Nematic liquid crystal. (b) Smectic liquid crystal (A type). (c) Cholesteric liquid crystal.

Liquid crystal phase will change with different temperature. The different alignment of liquid crystals accompany with the change of temperature can be expressed as follows:



The alignment of molecules will become isotropic and liquid when the temperature is higher than the clearing point, also called T_{N-1} . At this point, liquid crystal will become clear and transparent.

1.2.1 Nematic

The nematic phase is a kind of liquid crystal phase that most like the liquid. It's viscosity is small, response time is fast and it's the earliest liquid crystals that been used in LC TV, monitor, and all types of display elements [3,4]. It is characterized by molecules that has no positional order as in a liquid phase but has tenancy to point toward a same direction vector \mathbf{n} which is called the director and represents the statistically preferred direction. The molecules are aligned in parallel lines, but not in layers. The optical properties of nematic liquid crystals are similar to uniaxial crystals. The order parameter is the measurement of the degree of order in nematic phase.

$$S = \left\langle \frac{3}{2} \cos^2 \theta - \frac{1}{2} \right\rangle \quad (\text{eq. 1-1})$$

where θ is the deviation angle of each molecule from the director. The order parameter $S=0$ and $S=1$ means the substance is in isotropic phase and in isotropic phase, respectively. Generally, liquid crystal molecules have $0.5 < S < 0.7$.

1.2.2 Smectic

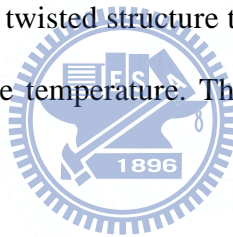
The smectic phase is close to the solid phase. Because of high viscosity and slow response time, smectic rarely been used in displays. Their main application is optical data storage materials.

Smectic liquid crystal molecules have one more degree of orientational order than nematic liquid crystal molecules. The molecules parallel to one another, forming a layer, but within the layer no periodic pattern exists. The liquid crystals are ordered in layers and normally float around freely inside these layers. The molecules tend to arrange themselves in

the same direction. There are several different sub-phases to describe smectic phase. The two best known of these are smectic A and smectic C. In the smectic A phase, the molecules align perpendicular to the layer planes, and in the smectic C phase the alignment of the molecules is at some arbitrary angle to the normal.

1.2.3 Cholesteric

In the cholesteric phase, the molecules are parallel and the layers are arranged in a helical, or spiral, fashion. The cholesteric liquid crystal phase is also called the chiral nematic liquid crystal phase. The name is historic as it goes back to the substances on which Reinitzer made his discovery. The molecules have the chiral centers and are in the nematic phase. They arrange themselves into a strongly twisted structure that often reflects visible light in different bright colors which depend on the temperature. They can therefore be used in temperature sensors.



1.3 Liquid Crystal Optics

When light passes through liquid crystals, it can have some effect like refraction, interference, diffraction, and polarization. Light is a kind of electromagnetic wave and has also can be divided into different kinds and colors by different wavelength. As a result, we will discuss only the monochromatic plane light wave in the following.

1.3.1 The Basic Properties of Light

From Maxwell equation, we can derive wave equation:

$$\vec{\nabla} \times (\vec{\nabla} \times \vec{E}) + \frac{1}{c^2} \frac{\partial^2 \vec{E}}{\partial t^2} = -\mu_0 \frac{\partial^2 \vec{P}}{\partial t^2} - \mu_0 \frac{\partial \vec{J}}{\partial t} \quad (\text{eq. 1-2})$$

For a generalized three dimensional monochromatic plane light wave, it propagate in a uniform dielectric substance, then $\vec{P} = \epsilon_0 \chi \vec{E}$ and $\vec{J} = 0$.

$$\vec{\nabla} \times (\vec{\nabla} \times \vec{E}) + \frac{n^2}{c^2} \frac{\partial^2 \vec{E}}{\partial t^2} = 0 \quad (\text{eq. 1-3})$$

The refraction index could be: $v = \frac{c}{n} \Rightarrow n \equiv \sqrt{\mu\epsilon}$

From eq. 1-3, we can get wave function as:

$$\vec{E}(\vec{r}, t) = \vec{A} \cos[\omega t - \vec{k} \cdot \vec{r} + \delta] \quad (\text{eq. 1-4})$$

Since light wave is transverse wave, we can define the direction of polarization is the direction of electric field. The direction of propagation is z, then the electric field of monochromatic plane light wave will vibrate in x-y plane.

Then we can rewrite eq. 1-4 as two vectors perpendicular with each other.

$$\begin{aligned} E_x &= A_x \cos(\omega t - kz + \delta_x) \\ E_y &= A_y \cos(\omega t - kz + \delta_y) \end{aligned} \quad (\text{eq. 1-5})$$

$A_x, A_y, \delta_x, \delta_y$, represents the amplitude of vibration and the phase individually. To describe the polarization of light wave simply, take $z=0$ to see the change of the vibration verses time on the x-y plane, then eq. 1-5:

$$\begin{aligned} E_x &= A_x \cos(\omega t + \delta_x) \\ E_y &= A_y \cos(\omega t + \delta_y) \end{aligned} \quad (\text{eq. 1-6})$$

We can define the phase as: $\delta = \delta_y - \delta_x$.

If $\delta = 0$ or π , then

$$E_y = \frac{A_y}{A_x} E_x \quad \text{or} \quad E_y = -\frac{A_y}{A_x} E_x \quad (\text{eq. 1-7})$$

From eq. 1-7, when the electric field direction of light vibrates in $\frac{E_y}{E_x}$ direction, we call it as linear polarization state. We use a new mathematical calculation way to describe the polarization state of light--- Normalized Jones Vector:

$$J = \frac{1}{\sqrt{A_x^2 + A_y^2}} \begin{pmatrix} A_x e^{i\delta_x} \\ A_y e^{i\delta_y} \end{pmatrix} \quad (\text{eq. 1-8})$$

When the light wave is linear polarized ($\delta = 0$ or π), the x axis has an included angle of ψ , then:

$$J_\psi = \begin{pmatrix} \cos \psi \\ \sin \psi \end{pmatrix} \quad (\text{eq. 1-9})$$

and

$$J_\psi * J_{\psi + \frac{\pi}{2}} = 0 \quad (\text{eq. 1-10})$$

So the two factors are orthogonal, and when $\psi = 0$:

$$J_x = \begin{pmatrix} 1 \\ 0 \end{pmatrix} \quad \text{and} \quad J_y = \begin{pmatrix} 0 \\ 1 \end{pmatrix} \quad (\text{eq. 1-11})$$

The index of J, means the x polarized direction and y polarized direction.

1.3.2 Light Waves Propagation in Uniaxial Medium

Most liquid crystal displays are nematic liquid crystal phase, if considering thin sliced nematic liquid crystal cell, we can take it as uniformed uni-axial medium.

In uni-axial medium, we have three refraction indexes as n_x , n_y , n_z .

When (1) $n_x = n_y = n_o$, and we call the index as ordinary index.

(2) $n_z = n_e$, we called the index as extraordinary index.

When $n_e > n_o$, define the medium as positive uni-axial medium; when $n_e < n_o$, define the medium as negative uni-axial medium.

Light propagate in uni-axial medium will separate to two propagate mode, one is ordinary wave, another is extraordinary wave. And we can present the two refractive indexes as:

$$\text{O wave : } \quad n = n_o \quad (\text{eq. 1-12})$$

$$\text{E wave : } \quad \frac{1}{n(\theta)^2} = \frac{\cos^2\theta}{n_o^2} + \frac{\sin^2\theta}{n_e^2} \quad (\text{eq. 1-13})$$

θ is the included angle of the propagate direction and z axis(light axis).

Consequently, when light propagate in this medium, the two directions of light will have different propagate velocity and different phase velocity. When light in the medium propagate for a while, the two parts of light will have phase retardation compare with each other. When the light passes through the medium, the two parts of light will combine together again, so the polarization happens. Therefore the birefringence wave plate uses this theorem to change the polarization of light.



Here are two examples:

I. When the direction of propagation along z axis(light axis):

$\theta = 0$, substitute into eq. 1-12 and eq. 1-13 :

$$\text{O wave : } n = n_o$$

$$\text{E wave : } n(0) = n_o$$

The two has the same phase velocity, $k_1 = k_2 = n_o \left(\frac{\omega}{c}\right)$ s. After light propagate in this two modes for a distance d, from eq. 1-4, the light does not have phase retardation. That means the polarization of light won't change.

II. When the direction of propagation along x-z plane:

From eq. 1-12 and eq. 1-13:

O wave : $n = n_o$, wave vector $k_o = n_o(\frac{\omega}{c})s$

E wave : $n_e(\theta) = \left[\frac{\cos^2\theta}{n_o^2} + \frac{\sin^2\theta}{n_e^2} \right]^{-1/2}$, wave vector $k_e = n_e(\theta)(\frac{\omega}{c})s$

From eq. 1-8 we know that, when light propagate in this medium for a distance d , O wave has a phase transition $n_o(\frac{\omega}{c})d$, E wave has a phase transition $n_e(\theta)(\frac{\omega}{c})d$, the two has a phase retardation Γ :

$$\Gamma = [n_e(\theta) - n_o](\frac{\omega}{c})d \quad (\text{eq. 1-14})$$

or

$$\Gamma = \frac{2\pi}{\lambda} [n_e(\theta) - n_o]d \quad (\text{eq. 1-15})$$

Phase retardation can change polarization of light propagation. Light propagate in the liquid crystals will change the phase because of the phase retardation and induce different light intensity passes through. By controlling the liquid crystals to change the light intensity is also the main function used in liquid crystal display.

(The equations in this section refer to “Elements of Photonics, Volume I: In Free Space and Special Media.”[5])

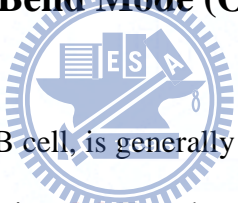
1.4 Operation Method of LCD

Generally, LC display can be seemed as two dimensional pixel alignments. Each pixel can be taken as a light switch, LC displays use liquid crystals to modulate the polarization of light wave and form a display element. It includes backlight mode, polarizer, LC cell, etc.. Since liquid crystal would react different when different electric field is applied. We can divide them into two groups, normally white and normally black. When no voltage applied, we named the LC cell tends to have the bright state as normally white, and LC cell tends to

have dark state as normally dark.

Take a normally white TN cell as our example of LCD operation. When un-polarized light irradiate from the back light, it would pass a polarizer first, leave the light that has the same polarized direction as polarizer's to enter the liquid crystal cell. When no electric field applied, the phase retardation leads LC cell to the bright state. When we applied an electric field on the LC layer, the z axis of liquid crystal would be parallel with the electric field. The phase retardation would be zero and the light can not pass through the analyzer. As a result, the LC cell would be the dark state. The grayscale is controlled by modulating the electric field.

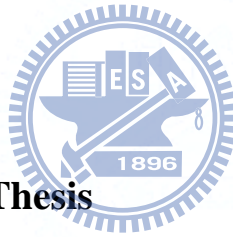
1.5 Optical Compensated Bend Mode (OCB)



The pi-cell, we also called OCB cell, is generally considered to be the fastest electro-optic response nematic liquid crystal device. [6] Together with the biaxial compensating film, this pi-cell is later improved and is also called the optical compensated bend (OCB) liquid crystal display. [7] The device comprises of parallel-rubbed alignment layer and nematic liquid crystal. It is aligned in splay state and operated in the bend state. The bend and splayed states are not topologically similar, so a nucleation process is required before the pi-cell can be operated. It typically takes a few seconds, and can be unreliable over large areas. The pi-cell has faster switching times than conventional nematic liquid crystal devices, capable of a combined on-off response time of fewer than 5 ms, due to lacking of backflow during director reorientation. It will be explained completely in Chapter 2.

1.6 Motivation and Objective

The optically compensated bend (OCB) cell, has strengths of wide viewing angles and fast response time less than 3 ms since there is no backflow involved in its' switching. Nevertheless, there are some drawbacks of OCB cell, for example, contrast ratio and it needs a long time of splay to bend transition. Techniques for fast splay to bend transition have received increasingly attention. Although aforementioned techniques successfully induced bend transition, most of the techniques sacrifice contrast ratio of the devices or needed a high pulse voltage to form the fast transition. The high voltage ($>10V$) is not suitable for TFT devices. In this study, we present a novel method to form bend transition cores which can spread uniformly in each pixel without applying the high pulse voltage and loosing of optic efficiency.



1.7 Organization of This Thesis

In this thesis, the overview of OCB cells will be introduced in chapter 2. Then, in chapter 3, the measurement systems adopted in this experiment were described. The experimental fabrication processes, characteristics measurement, results and discussions are in Chapter 4. Finally, Conclusions were drawn in Chapter 5 along with future research directions pointed out.

Chapter 2

Overview of OCB Cell

2.1 Characteristics of OCB Cell

The optically compensated bend (OCB) cell [8,9], also known as pi-cell, has strengths of wide viewing angles[10] and fast response time[6] less than 3 ms since there is no backflow involved in its' switching. [11, 12] Nevertheless, there are some drawbacks of OCB cell, for example, contrast ratio and phase transition. OCB cells will initially stable at the splay state. The transition is needed to operate in the bend state. The voltage higher than critical voltage is required to transform the phase from splay state to bend state.

2.1.1 OCB Cell Structure

Fig. 2-1 shows the structure of the π cell. Two crossed polarizer are above and under the cell, and the alignment layers have the same rubbing direction. The rubbing direction and polarizer transmittance direction have an angle of 45 degree. In general, the pretilt angle of the alignment layer used in π cell is about in the range of 6~14 degree.

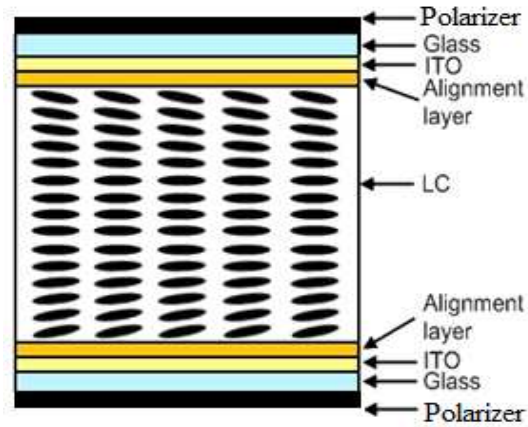


Fig. 2-1 The structure of the π cell.

2.1.2 Wide Viewing Angle

From [Fig. 2-2](#), we can see that when the transmittance is 50%, the curve of TN mode has asymmetric distribution, while the curve of π cell has symmetric distribution. This phenomenon is related to the alignment of LC molecules. Because in the plane of rubbing direction, the alignment of LC molecules is symmetric in the vertical direction, so we will experience the same optical path along the symmetric direction in this plane ([Fig. 2-3](#)). There is self-compensated effect in this direction. Therefore, the horizontal viewing angle of π cell is wider and symmetric than TN mode.

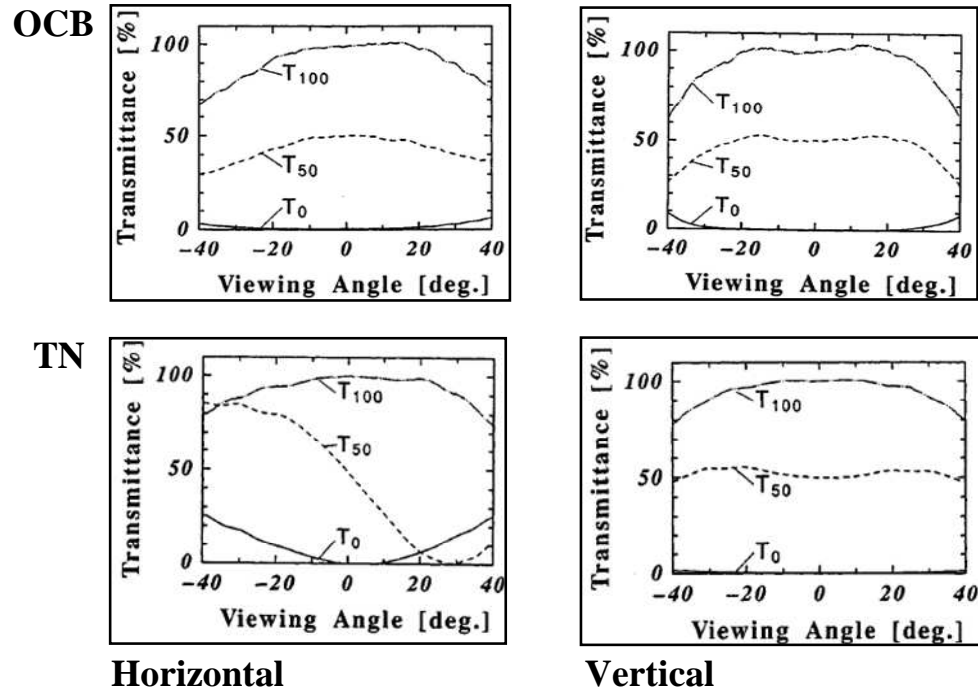


Fig. 2-2 Experimental results of the viewing angle dependent transmittance for TN cell and OCB cell [13].

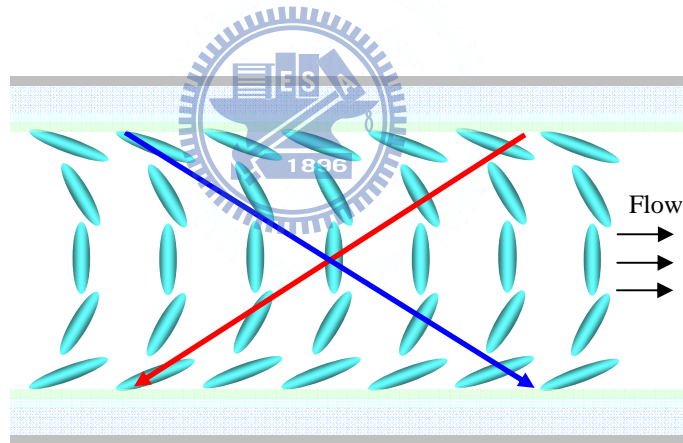


Fig. 2-3 Cross-section view of OCB cell.

2.1.3 Fast Response Time

One of the famous advantages of OCB cell is fast response [6]. OCB cell operates in bend mode as Fig. 2-4 (b) and homeotropic state as Fig. 2-4 (c). Since the topographically geometry between these two states is similar, the response time is fast. From Fig. 2-5, the LC molecules will rotate in the same direction when switch, we called that flow effect. As a result, when removed the voltage, the response time is about 1 to 10ms, faster than TN mode (50 ms)

and the response of human eyes (20 ms).

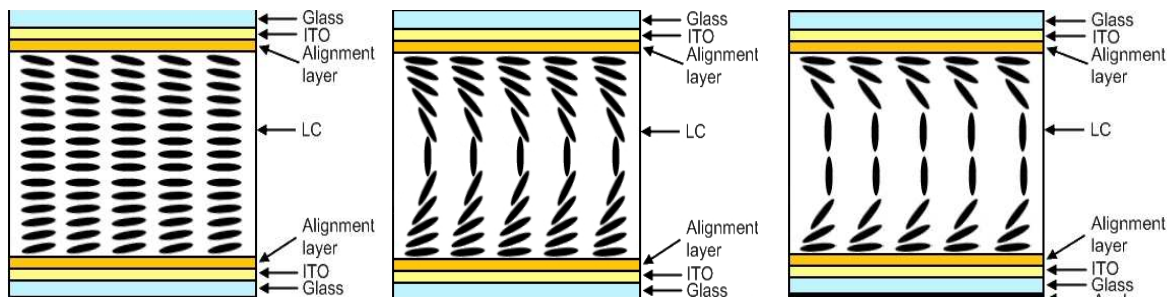


Fig.2-4 (a)

Fig.2-4 (b)

Fig.2-4 (c)

Fig. 2-4 (a) splay state, (b) Vcr, bend mode, and OCB cell is in the bright state. (c) Von, homeotropic state, and OCB cell is in the dark state.

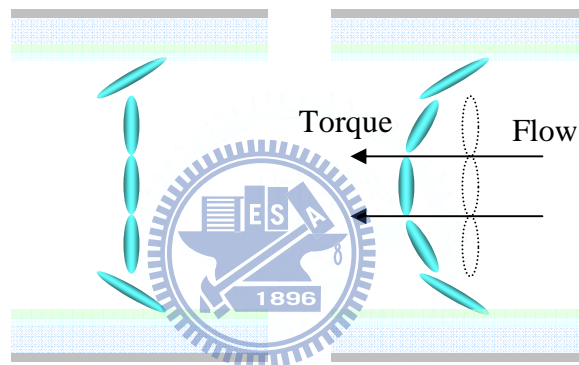


Fig. 2-5 Schematic figure of the dynamics in the π cell. The flow induces the torque to accelerate to relax.

2.1.4 Phase Transition Mechanism

The liquid crystal geometry and the commonly known states in parallel-rubbed nematic device are shown in Fig. 2-6 There are five important configurations in pi-cell operation: the splayed ground state (H), the symmetric splay state (Hs), the asymmetric splay state (Ha), the bend state and the 180° twist state. [14, 15, 16]

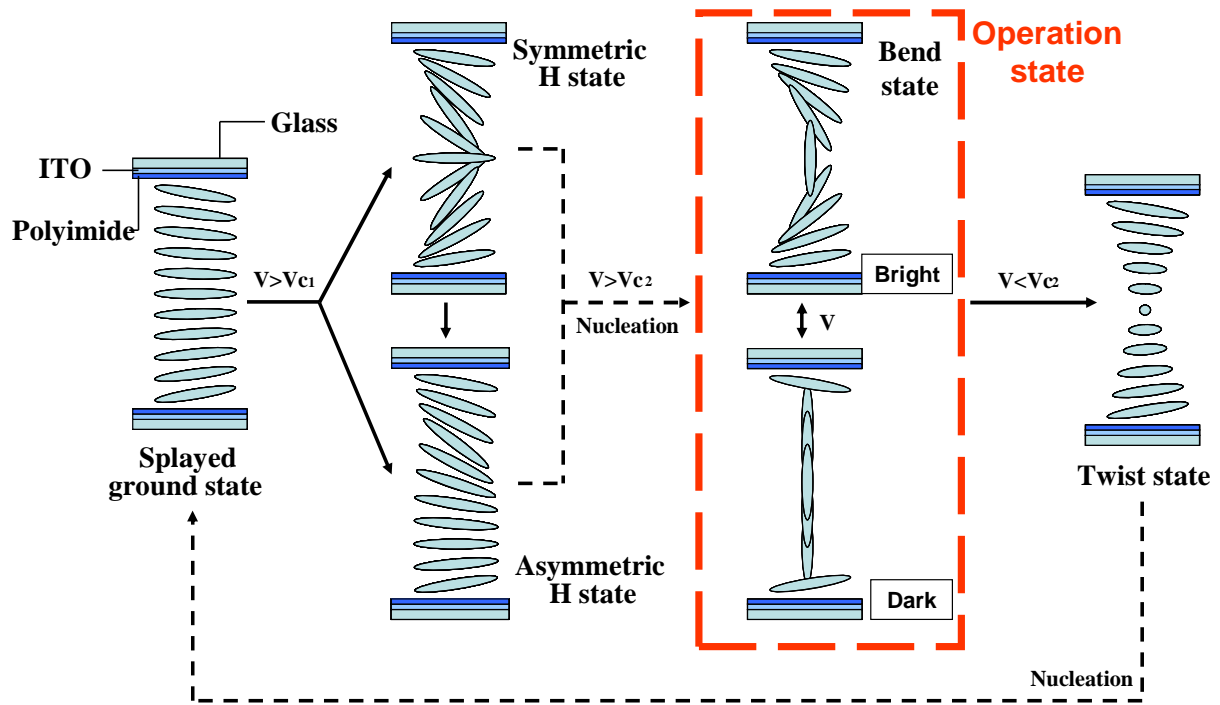


Fig. 2-6 Five configurations of pi-cell. Dotted lines indicate nucleation processes.

When no voltage applied, the most stable state is splayed ground state. The H state is a transient state that forms during sudden voltage above a critical voltage, V_{C1} which is around $1 V_{rms}$ for most materials, applied to the splayed ground state. If the director tilt angle on both surfaces is identical, the device switches into the Hs (symmetry splayed) transient state. Any imbalance of surface tilt results to Ha (asymmetry splayed) transient states. As the voltage is further increased to above a critical voltage V_{C2} , which is around $2 V_{rms}$ for most materials, the bend state becomes more stable state. The bend state is topologically distinct from the splay state and its transient states. To achieve the uniform bend state from splay state, nucleation process is required and the process will takes few seconds to minutes to complete. If the voltage is fall below V_{C2} the device will relax to the twist state and further nucleation into the splayed ground state.

To improve the problem of phase transition, the common method likes to increase pretilt angle[17,18], generate bend core or chiral dopant[19,20], multi-dimensional alignment[21],

offer a twist electric field[22], polymer stabilized[23, 24]...etc. Although these method can shorten the transition time from splay state to bend state, but they usually affect other optical properties (ex. worse the dark state), or the fabrication process, driving method become complicated, make the π cell lose its predominance.

2.2 Nucleation

Nucleation is the extremely localized budding of a distinct thermodynamic phase. Some examples of phases that may form via nucleation in liquids are gaseous bubbles, crystals, or glassy regions. Nucleation normally occurs at nucleation sites on surfaces contacting the liquid or vapor. Suspended particles or minute bubbles also provide nucleation sites. This is called heterogeneous nucleation. Nucleation without preferential nucleation sites is homogeneous nucleation. Homogeneous nucleation occurs spontaneously and randomly, but it requires superheating or supercooling of the medium.

2.2.1 Nucleation Theory

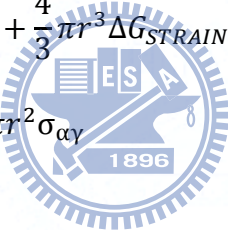
Nucleation theory can divide into two parts, one is homogeneous nucleation, and another is heterogeneous nucleation.

I. Homogeneous nucleation

Nucleation generally occurs with much more difficulty in the interior of a uniform substance, by a process called homogeneous nucleation. The creation of a nucleus implies the formation of an interface at the boundaries of a new phase.

This change in free energy is balanced by the energy gain of creating a new volume, and the energy cost due to creation of a new interface. When the overall change in free energy, ΔG is negative, nucleation is favored. Some energy is consumed to form an interface, based on the surface energy of each phase. If a hypothetical nucleus is too small (known as an unstable nucleus or "embryo"), the energy that would be released by forming its volume is not enough to create its surface, and nucleation does not proceed. The critical nucleus size can be denoted by its radius, and it is when $r=r^*$ (or r critical) that the nucleation proceeds.

For example, in the classic case [25] of a spherical cluster, considering the homogeneous nucleation of α from γ . For a spherical particle of radius r with an isotropic interfacial energy $\sigma_{\alpha\gamma}$, the change in free energy as a function of radius is:

$$\begin{aligned}\Delta G &= \frac{4}{3}\pi r^3 \Delta G_{CHEN} + \frac{4}{3}\pi r^3 \Delta G_{STRAIN} + 4\pi r^2 \sigma_{\alpha\gamma} \\ &= \frac{4}{3}\pi r^3 G_V + 4\pi r^2 \sigma_{\alpha\gamma}\end{aligned}\quad (\text{eq. 2-1})$$


Where $\Delta G_{CHEN} = G_V^\alpha - G_V^\gamma$, G_V is the Gibbs free energy per unit volume of α and G_{STRAIN} is the strain energy per unit volume of α . The first term shows the energy gain of creating a new volume and the second term shows the energy loss due to surface tension of the new interface. The variation in ΔG with size is illustrated in Fig. 2-7.

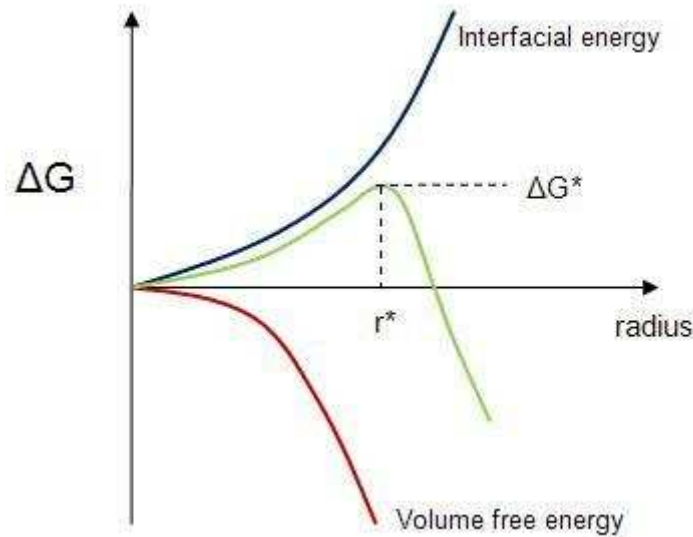


Fig. 2-7 The activation energy barrier ΔG^* and the critical nucleus size r^* according to classical nucleation theory based on heterophase fluctuations.[26]

Because of $dG/dr > 0$, it costs free energy to add molecules to this cluster until the radius reaches

$$r^* = -\frac{2\sigma}{G_V} \quad (\text{eq. 2-2})$$

Where $dG/dr = 0$

Addition of new molecules to clusters larger than this critical radius releases, rather than costs, available work. In other words at that point growth of the cluster is no longer limited by nucleation, but perhaps by diffusion [27] or by reaction kinetics instead. Substitute eq. 2-2 to eq. 2-3, we can find the free energy needed to form this critical radius by

$$\Delta G^* = \frac{16\pi\sigma^3}{3G_V^2} \quad (\text{eq. 2-3})$$

which occurs at the maximum ΔG where $dG/dr = 0$.

As the phase transformation becomes more and more favorable, the formation of a given volume of nucleus frees enough energy to form an increasingly large surface, allowing

progressively smaller nuclei to become viable.

II. Heterogeneous nucleation

Heterogeneous nucleation occurs much more often than homogeneous nucleation. It forms at preferential sites such as phase boundaries or impurities like dust and requires less energy than homogeneous nucleation. Fig. 2-8 shows the difference in energy barriers of homogeneous and heterogeneous nucleation and the critical radius remains unchanged.

At such preferential sites, the effective surface energy is lower, therefore diminished the free energy barrier and facilitating nucleation. Surfaces promote nucleation because of wetting – contact angles greater than zero between phases encourage particles to nucleate. The free energy needed for heterogeneous nucleation is equal to the product of homogeneous nucleation and a function of the contact angle:

$$\Delta G_{heterogeneous} = \Delta G_{homogeneous} f(\theta) \quad (\text{eq. 2-4})$$

where $f(\theta) = \frac{1}{2} - \frac{3}{4} \cos\theta + \frac{1}{4} \cos^3\theta$.

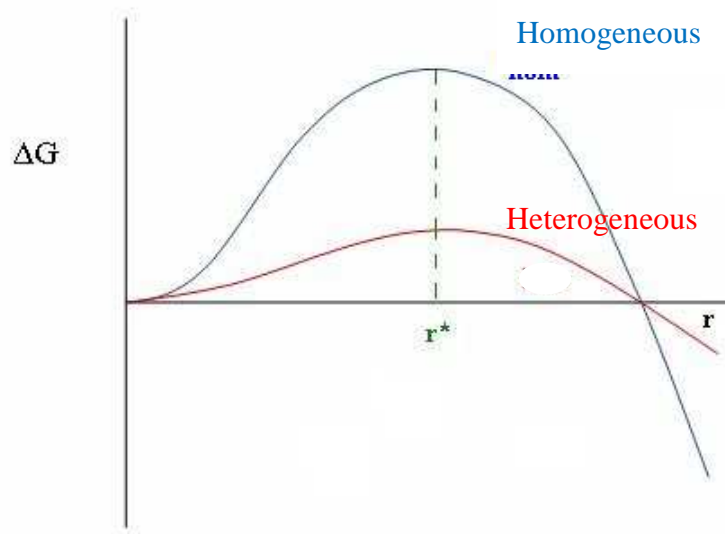


Fig. 2-8 Difference in energy barriers of homogeneous and heterogeneous nucleation.[26]

The barrier energy needed for heterogeneous nucleation is reduced. The wetting angle determines the ease of nucleation by reducing the energy needed. However, the volume can be significantly less for heterogeneous nucleation due to the wetting angle affecting the shape of the cluster. In the case of heterogeneous nucleation, some energy is released by the partial destruction of the previous interface.

In our case, the nucleation process occurred when applying voltage to liquid crystal cell. The heterogeneous nucleation theory was considered. In chapter 4, the experiment results and heterogeneous nucleation theory will be discussed.

2.2.2 Nucleation Rate



The nucleation rate, I , depends on the average number of critical clusters, n^* and the diffusion of molecules to the cluster, β .

$$I = n^* \beta \quad (\text{eq. 2-5})$$

Where the average population of critical nuclei is

$$n^* = N \exp\left(\frac{-\Delta G^*}{k_B T}\right) \quad (\text{eq. 2-6})$$

Where :

ΔG^* : critical free energy needed

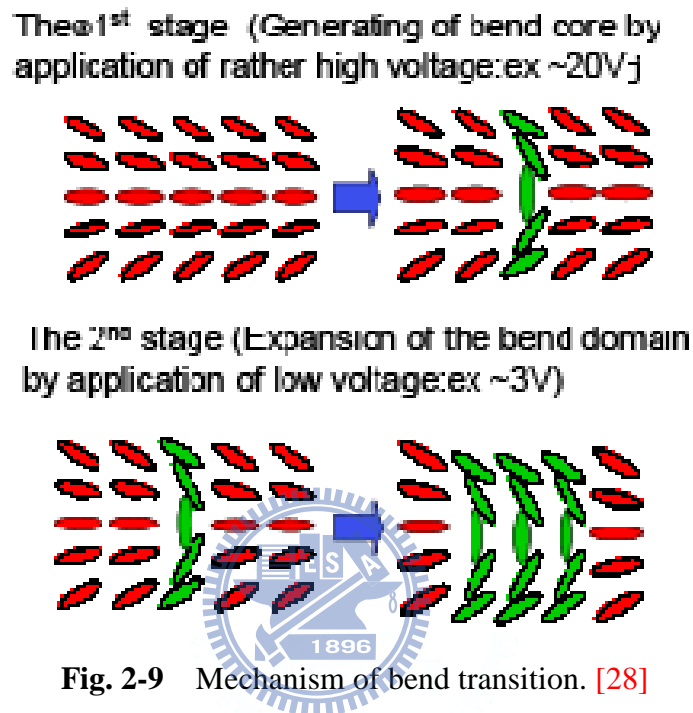
N : the number of potential nucleation sites per unit volume

k_B : the Boltzmann constant

2.2.3 Review the Study of Nucleation in OCB cell

It is found that the transition in OCB cell can divide into two stages as Fig. 2-9 shown.

[28] It shows that the generation of a bend core is essential. [29, 30]



The OCB cell is in the splayed ground state when no voltage is applied, where the liquid crystal molecules are all aligned with the rubbing direction. The splayed ground state must be switched into an operating bend state by applying a high voltage across the cell. Because of the topology of these states are different, the transition starts with breaking the anchoring symmetry at the cell surfaces and forming a bend domain with a disclination loop around it. The transition is through the nucleation and movement of disclination lines. In the simulation by P. J. Bos *et al.*, it clearly demonstrate it. [29] After the region of concentrated splay distortion is formed, the order parameter starts to decrease in that region. Each of the original defect cores evolve to a pair of $-1/2$ and $+1/2$ disclination lines moving away from each other toward other defect lines with the opposite sign as Fig. 2-10 shown. Two portions of the

disclination loop that run perpendicular to the rubbing direction are regarded as a pair of wedge disclination lines. The bend nucleation process, which is associated with the liquid crystal physical properties and the cell fabrication process parameters, is relatively easy to observe the movement of the disclination lines as a growth rate of bend domains under different conditions.

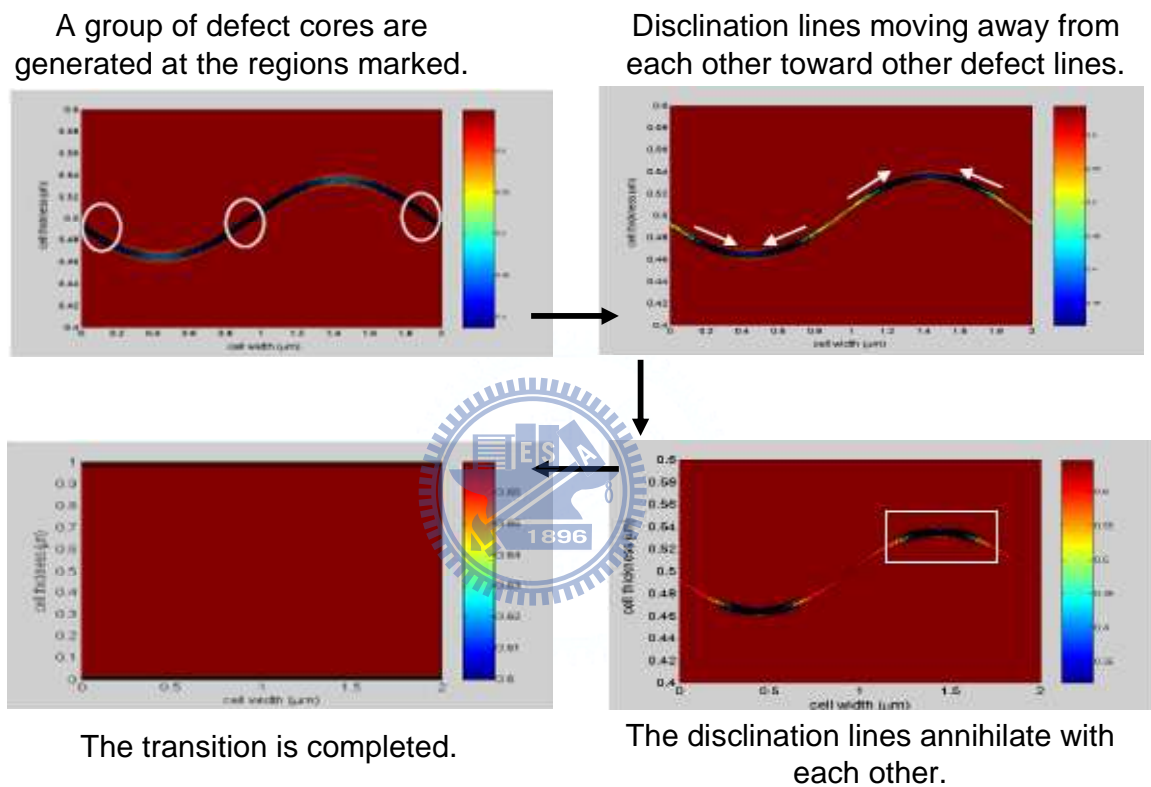


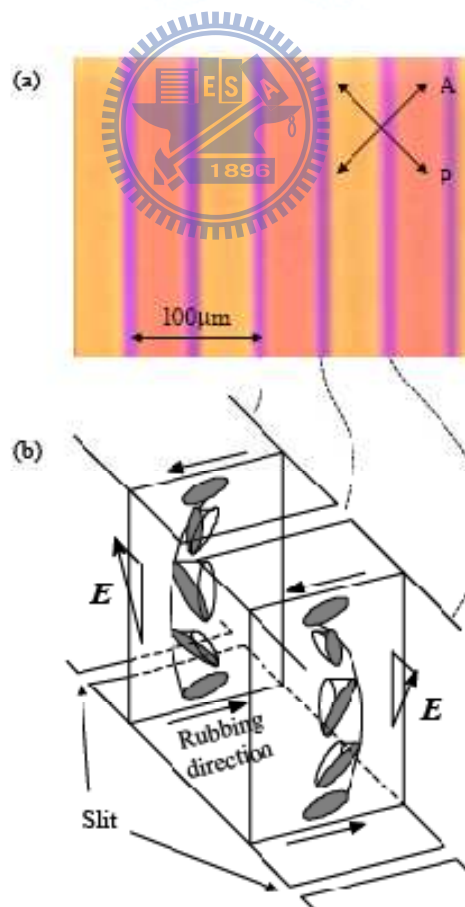
Fig. 2-10 Order parameter profile of simulation. [29]

J. Cheng *et al.* studied the switching process between the bend state and the splay state in a bistable nematic device. [31] The energy difference of the two states can be obtained in a simple formulation, assuming a “boundary-layer model.” The velocity of the disclination lines motion can be calculated from the energy difference and the damping factor. The topology of the cell is varied from the splay state to the bend state, and the declination lines finally annihilate with each other when the transition is completed.

The bend state is the operation state in pi-cell, as a result, many nucleation techniques have been proposed to induce splay to bend transition. These methods can be categorized into chiral and non-chiral doped LC systems.

I. With chiral doping LC systems

For chiral doping LCs system, chiral doping molecules were utilized to stabilize a 180° twist configuration to eliminate the required bend nucleation.[32,33] The technique eliminates the requirement for nucleation of bend state by using the 180° twist configuration is similar to the bend state at high voltage. Further enhancement with slits and protrusions on the substrates can be seen in Dual-Domain Bend Mode (DDB Mode) LC devices. [34]



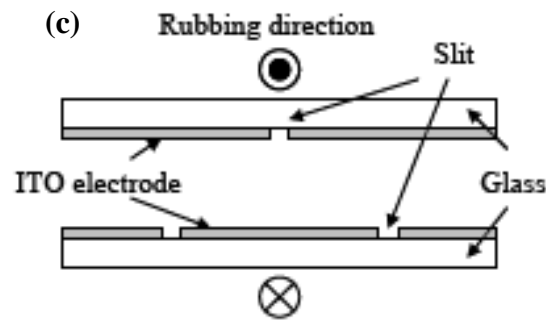


Fig. 2-11 (a) Microscopic image of DDB cell. (b) Schematic diagram of the director profile of each domain. (c) Cross-sectional structure of DDB cell. [34]

II. Without chiral doping LC systems

Voltage nucleation and stabilization is the basic method for nucleation by using a high pulse ($>10V$). however, it is not suitable for TFT-drivers. [35, 36] On the other hand, the non-chiral doping system is stressed on creating bend transition cores to reduce transition time in OCB cell. Bend transition cores can be generated by defects and structures such as spacers. [37] Under application of a voltage, anisotropic structures around the spacers by adsorption are able to nucleate the bend state. Fig. 2-12 shows that high pre-tilt angles were used to stabilize the bend state at 0V. [38, 39] The alignment layers of about 45° pre-tilt angles make pi-cells in the bend alignment with no bias voltage. [40, 41, 42] The relaxation times are increased and the electro-optic modulation is reduced at high surface tilt angles. As the result, the multi-domain alignment method is accessed. [43, 44, 45] In this method, as Fig. 2-13 shown, the transition cores were created by high tilt angle alignment region.

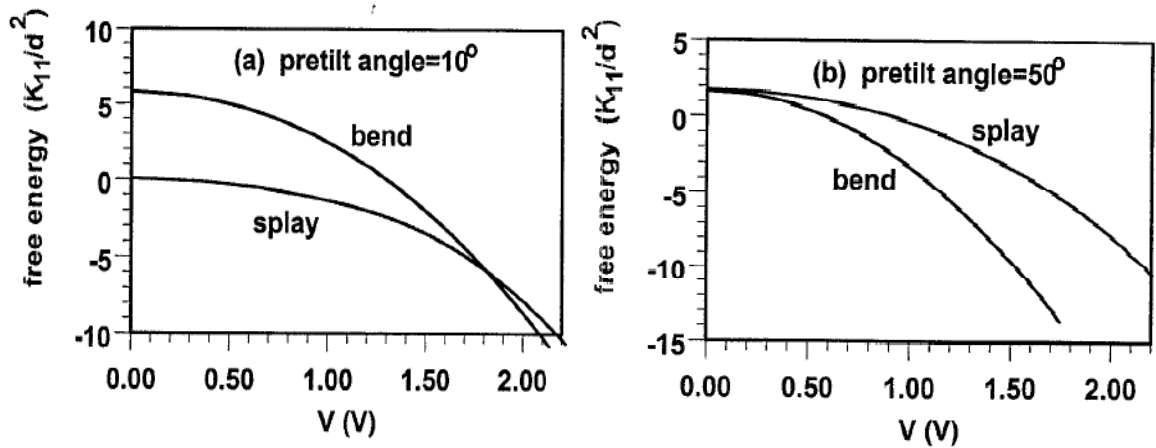


Fig. 2-12 Free energy of the bend and splay configurations vs. applied voltage in the pi-cells. [38]

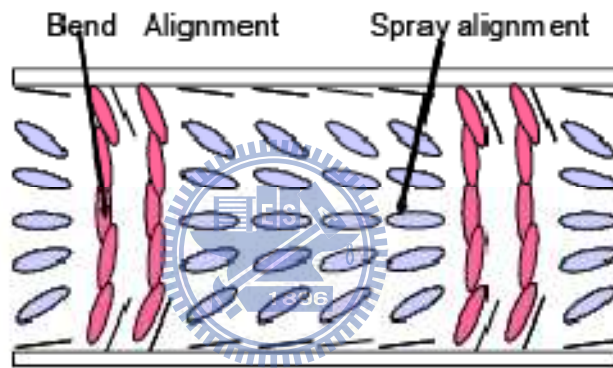


Fig. 2-13 The scheme of high tilt angle alignment cell. [28]

Network polymerization is a method to prevent the return of the splay state at low voltages. (Fig. 2-14) [46, 47] With polymer walls, an initial splay-to-bend transition is unnecessary. But it is difficult to overcome the ionic contamination and possible image sticking.

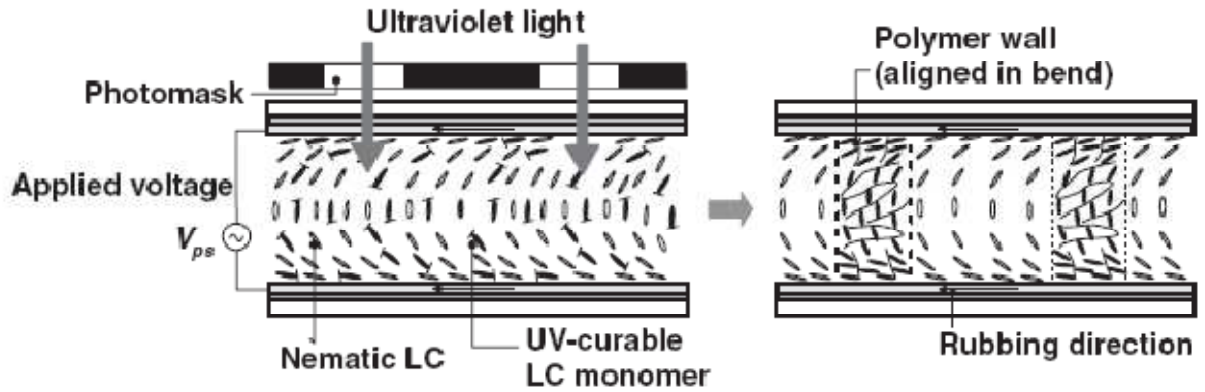


Fig. 2-14 Schematic diagram of polymer wall. [46]

2.3 Summary

The nucleation process and phase transition in OCB cell were introduced in this section. Many nucleation enhancement techniques had been proposed to induce splay to bend transition and reduce the transition time. The simplest method was to apply a high voltage pulse (20~30V) to induce the bend state formation. However, the method is not suitable for all TFT-driving devices. Other methods can be categorized into chiral and non-chiral doped LC systems. In this study, a novel method to achieve fast and uniform transition in each pixel without losing optic efficiency was presented.

Chapter 3

Measurement Systems

3.1 Introduction

The instruments which are available to characterize the parameters of liquid crystal test cells will be introduced in this chapter. The surface morphology was inspected by atomic force microscope (AFM). The cell gap of an empty cell was measured by interferometric method. Instruments such as polarizing optical microscope (POM), and laser optical system were utilized to characterize textures, and electro optical characteristics, respectively. The major features of the above mentioned instruments will be illustrated in the chapter.

3.2 Atomic Force Microscope (AFM)

The atomic force microscope (AFM) consists of a flexible micro-scale cantilever with a scanning sharp tip at its end that is used to scan the specimen surface. The cantilever is typically silicon or silicon nitride with a tip radius of curvature on the order of nanometers. The tips typically have an end radius of 2 nm to 20 nm, depending on tip type. When the tip is brought into proximity of a sample surface, forces between the tip and the sample lead to a deflection of the cantilever according to Hooke's law. Depending on the situation, forces that are measured in AFM include mechanical contact force, Van der Waals forces, capillary forces, chemical bonding, electrostatic forces, magnetic forces, Casimir forces, solvation forces etc.

Typically, the deflection is measured using a laser spot reflected from the top of the cantilever into an array of photodiodes. The scanning motion is conducted by a piezoelectric tube scanner which scans the tip in a raster pattern with respect to the sample (or scans to the sample with respect to the tip). The tip-sample interaction is monitored by reflecting a laser off the back of the cantilever into a split photodiode detector. By detecting the difference in the photo-detector output voltages, changes in the cantilever deflection or oscillation amplitude are determined. The schematic diagram of this mechanism is depicted in Fig. 3-1.

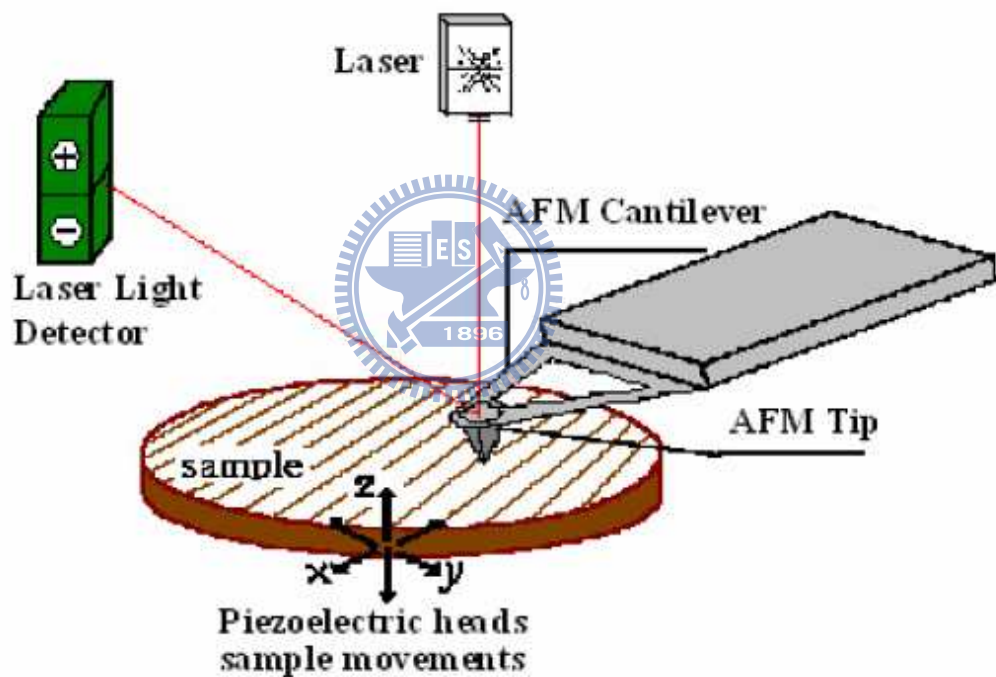


Fig. 3-1 Concept of AFM and the optical lever.

There three major operation made for AFM :

I. Contact mode

Contact mode is the most common method to operate the AFM. But as the term

suggests, the tip and the sample remain in close contact as scanning proceeds at this mode. It consists of scanning the probe across a sample surface while monitoring the change in cantilever deflection with the split photodiode detector. A feedback loop maintains a constant cantilever deflection by vertically moving the scanner to maintain a constant photo-detector difference signal. The distance the scanner moves vertically at each x, y data point is stored by the computer to form the topographic image of the sample surface. This feedback loop maintains a constant force during imaging, which typically ranges between 0.1 to 100 *nN*.

II. Non-contact mode

Non-contact operation is another method which may be employed when imaging by AFM. The cantilever must be oscillated above the surface of the sample at such a distance that we are no longer in the repulsive regime of the inter-molecular force curve. This is a very difficult mode to operate in ambient conditions with the AFM.

III. Tapping mode

It is the next common mode used in AFM. The cantilever is oscillated at its resonance frequency (typically ~ 300 *kHz*) and positioned above the surface so that it only taps the surface for a very small fraction of its oscillation period when operated in air or other gases. The laser deflection method is used to detect the root-mean-square (RMS) amplitude of cantilever oscillation. A feedback loop maintains a constant oscillation amplitude by moving the scanner vertically at every x, y data point. Recording this movement forms the topographical image. This is still contact with the sample in the sense defined earlier, but the very short time over which this contact occurs means that lateral forces are dramatically reduced as the tip scans over the surface. The advantage of tapping mode over contact mode is

that it eliminates the lateral, shear forces present in contact mode, enabling tapping mode to image soft, fragile, and adhesive surfaces without damaging them, which can be a drawback of contact mode AFM. In this thesis, the tapping mode AFM was used.

3.3 Cell Gap Measurement System

For liquid crystal display, the thickness of cell gap has significant influence in optical performance. Thus, every time before the infection of liquid crystal the empty cell gap must be measured and the interferometric method [48] is used. The measurement instrument is UV/Vis spectrophotometer Lambda 650 from Perkin Elmer, and the principle of this method is introduced as below.

UV/Vis spectrophotometer Lambda 650 Perkin Elmer as shown in Fig. 3-2 is operated in the ultraviolet visible spectral ranges (190 nm – 900 nm) with the resolution ≤ 0.17 nm, and the spectrometer features a double-beam, double monochromator, and ratio recording optical system. The instrument is usable in a wide range of applications as indicated by the performance specifications. Absorption and transmittance of materials can be characterized with Lambda 650, and the large cavern supposes the space for polarizers and other expanded object.



Fig. 3-2 The picture of LAMBDA 650 PerKin Elmer.

The basic concept of the measurement method is based on the interference pattern of the light reflected by a layer with two reflecting surfaces. The illustration is as Fig. 3-3. Define the coefficient of reflection R_1 as the ratio of the light reflected by surface 1 to the total incident light on surface 1, and R_2 is the reflection coefficient of surface 2. We assume that the total incident light is $I = \cos \omega t$ and no absorption of light in surface 1 and 2. The total reflected light R is

$$R = R_1 \cos \omega t + \sum_{k=1}^{\infty} R_1^{k-1} R_2^k (1 - R_1)^{1+k} \cos \omega(t - kt_0) \quad (\text{eq. 3-1})$$

where $\omega = 2\pi c n_{gap}^{1/2} / \lambda$ and $t_0 = 2d_{gap} n_{gap}^{1/2} / c$, c is the speed of light in vacuum, λ is the wavelength, d_{gap} is the thickness of the layer, and n_{gap} is the refractive index of the layer.

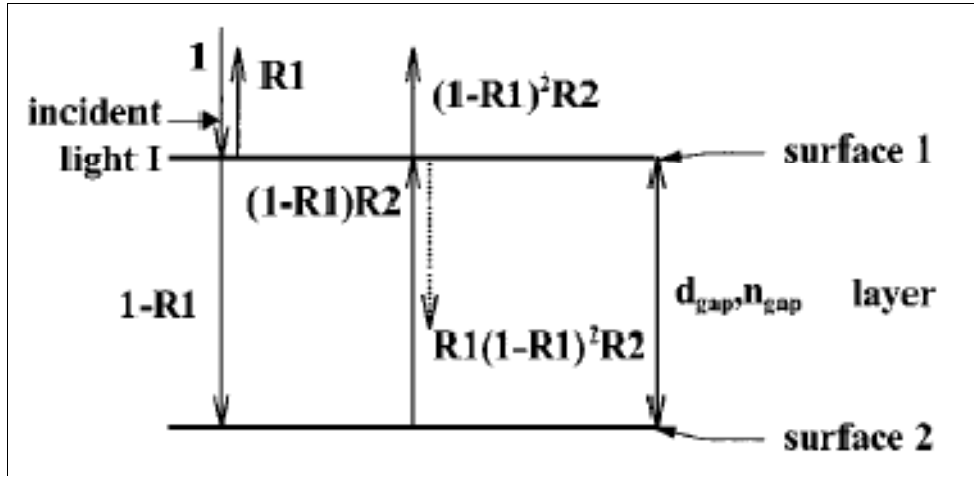


Fig. 3-3 Two reflecting surfaces separated by a layer causing light interference. The dotted line indicates the first internal reflection. [48]

The cosine factors in eq. 3-1 for $k > 1$ are caused by internal reflections. Since $R_1 < 1$ and $R_2 < 1$, the magnitude of the cosine factors for $k > 1$ is much smaller than for $k = 1$. Therefore we neglect the internal reflections, so

$$R = R_1 \cos \omega t + (1 - R_1)^2 R_2 \cos \left(\omega t - \frac{4\pi n_{gap} d_{gap}}{\lambda} \right) \quad (\text{eq. 3-2})$$

Thus the reflected spectrum is

$$|R(\lambda)|^2 = R_1^2 + [(1 - R_1)^2 R_2]^2 + 2R_1(1 - R_1)^2 R_2 \times \cos(4\pi n_{gap} d_{gap} / \lambda) \quad (\text{eq. 3-3})$$

The periodic term in eq. 3-3 causes what is generally known as an interference pattern. The periodicity of the reflected interference spectrum determined the optical thickness of the cell gap, $n_{gap} d_{gap}$.

If for instance λ_1 and λ_2 are two wavelengths yielding extrema in eq. 3-3, then $\cos(4\pi n_{gap} d_{gap} / \lambda) = \pm 1$ for $\lambda = \lambda_1$ and $\lambda = \lambda_2$. So

$$2n_{gap} d_{gap} = k_1 \lambda_1 / 2 \quad (\text{eq. 3-4})$$

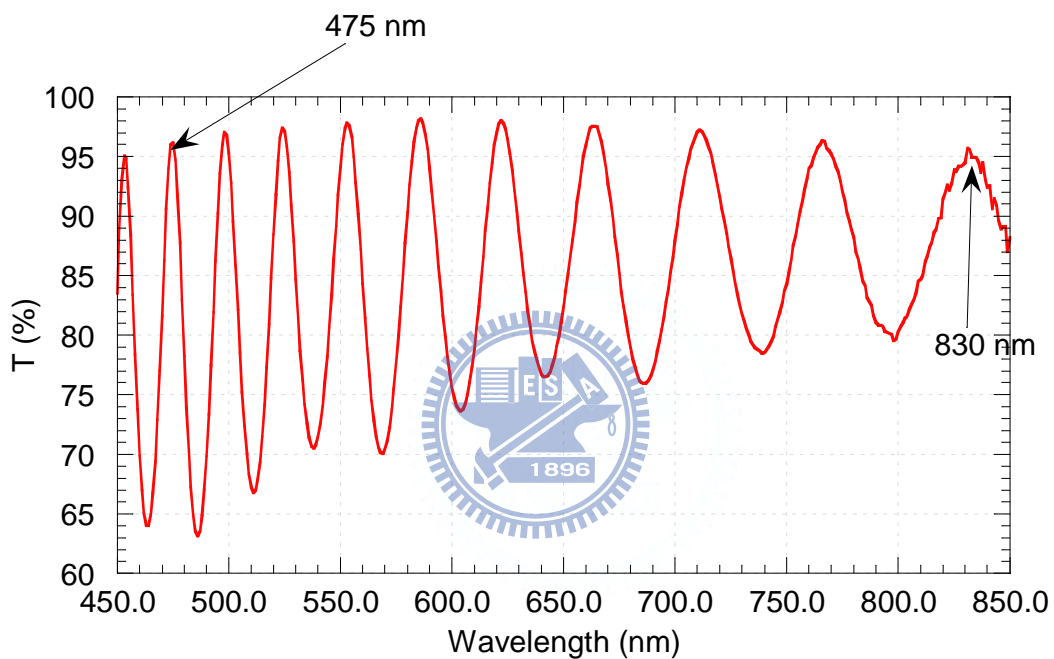
$$2n_{gap} d_{gap} = k_2 \lambda_2 / 2 \quad (\text{eq. 3-5})$$

where k_1 and k_2 are the natural numbers. Suppose $\lambda_1 > \lambda_2$, then $k_2 = k_1 + x$, where x is a natural number. Then,

$$n_{gap}d_{gap} = \frac{x\lambda_1\lambda_2}{4(\lambda_1 - \lambda_2)} \quad (\text{eq. 3-6})$$

and the value of $x-1$ indicates the number of extrema in $|R(\lambda)|^2$ between two wavelength λ_1 and λ_2 .

Fig. 3-4 shows the measurement of one test cell, and the cell gap was determined from eq. 3-6.



$$n_{gap}d_{gap} = \frac{x\lambda_1\lambda_2}{4(\lambda_1 - \lambda_2)} = \frac{18 \times 830 \times 475}{4 \times (830 - 475)} = 5\mu\text{m}$$

Fig. 3-4 Example of cell gap measurement.

3.4 Polarizing Optical Microscope (POM)

The polarized optical microscope is designed to observe and photograph specimens that are visible primarily due to their optically anisotropic character. In order to accomplish this task, the microscope must be equipped with both a polarizer, positioned in the light path

somewhere before the specimen, and an analyzer (a second polarizer), placed in the optical pathway between the objective rear aperture and the observation tubes or camera port. Image contrast arises from the interaction of plane-polarized light with a birefringent specimen to produce two individual wave components that are each polarized in mutually perpendicular planes. Liquid crystal microphotographs were observed under POM, Olympus BX51 as shown in Fig. 3-5, the magnifications of POM are 100X, 200X, 500X and 1000X with changeable object lens of 10X, 20X, 50X and 100X, respectively, and a 10X eyepiece. Two measurable modes depend on transparent and reflective substrates are utilized with bottom light source and top light source, respectively. And adjustable and movable polarizer can be utilized in both modes. Images observed under POM can be captured under CCD, and the parameters such as distance, area and angle can be calculated with its software.



Fig. 3-5 The picture of POM Olympus BX51.

3.5 Laser Optics System

The laser optical system was used for the measurement of electro-optical properties, such as V-T characteristics and response time. This system is shown in Fig. 3-6. The test cell was placed between a polarizer and an analyzer. The light source is He-Ne laser. A 10% ND filter is used for reducing the intensity of laser source to fulfill the intensity within the acceptable range of the photo detector. The test cell was driven by a waveform generator WFG500 from FLC Electronics AB which is connected with computer through GPIB interface. WFG500 is multi-channel high voltage waveform generator. It is powerful to be a high voltage signal generator with 8 output channels and waveform-designed ability. Any waveforms even they are not regular can be designed with the maximum output voltage for $\pm 100V$ and the minimum designable pulse width for 200ns. The optical signals were received by photo detector PIN 20 from FLC Electronics AB. The light sensitive component, silicon PIN photo-diode contributes to a good compromise between sensitivity and speed, and the signal with its response more 40ns can be detected by this instrument. The photo detector would transform the intensity of laser light into voltage, and were exhibited with oscilloscope or multimeter.

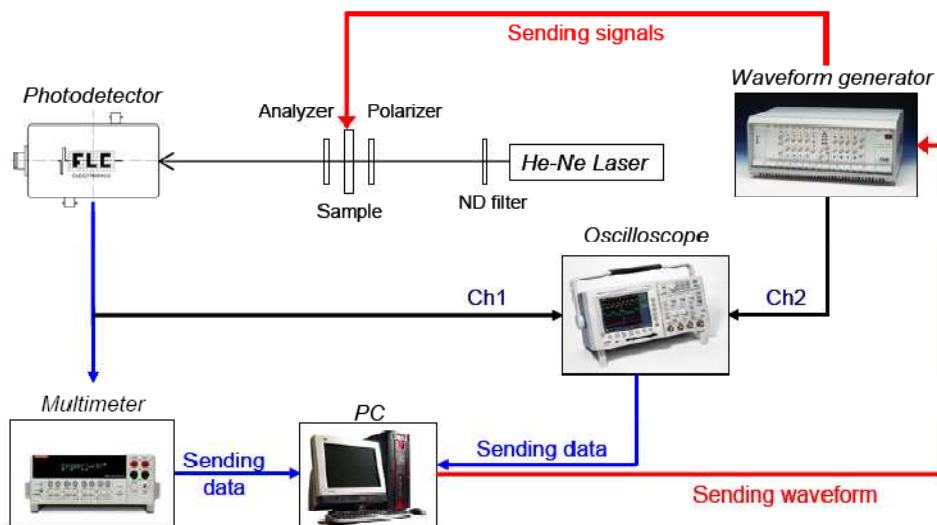


Fig. 3-6 Schematic of the laser optics system.

Chapter 4

Experimental Results and Discussion

4.1 Introduction

It is well known that the operating state (bend state) of OCB cells must be nucleated then uniformly spread the bend orientation in splay state before operation. In this study, the random distribution of silicon oxide nano-particles has been investigated for decreasing the time of splay-to-bend transition in OCB cells. The relationship between transition time and nano-particle distribution rate in hetero-nucleation was discussed. The electro-optical properties were characterized with optical system. Transition time was measured by digital-camera. In order to achieve uniform nano-particle distribution, three kinds of mixture solutions were proposed here. Under the optimum conditions, the 99.9% reduction of splay-to-bend transition time was found in nanostructure structure treated surfaces. Here are the mixture solution systems:

I. Nano-particle in DI water

In this solution, the Silicon oxide (SiO_2) nano-particle aqueous solution (90 nm, mean diameter) was diluted with de-ionic (DI) water.

II. Nano-particle in PVA(Polyvinyl Alcohol) solution

The mixture solution consisted of SiO₂ nano-particle aqueous solution (90 nm, mean diameter), DI water, PVA and Alcohol. The ratio of PVA and alcohol in the mixture solution were 2.5wt% and 5wt%, respectively.

III. Nano-particle in Ethylene Glycol (EG) and Propylene glycol monomethyl ether acetate (PGMEA) mixed solution

In this solution, two diameters (50nm and 90nm) of SiO₂ nano-particle were used here. The mixture solution consisted of SiO₂ nano-particle aqueous solution, DI water, EG (Ethylene Glycol) and PGMEA (Propylene glycol monomethyl ether acetate). Fig. 4-9 shows the diagram of mixed method. The EG (Ethylene Glycol) and PGMEA (Propylene glycol monomethyl ether acetate) were mixed at a weight ratio of 9:1 and at a total concentration of 60wt% added to SiO₂ nano-particle aqueous solution.

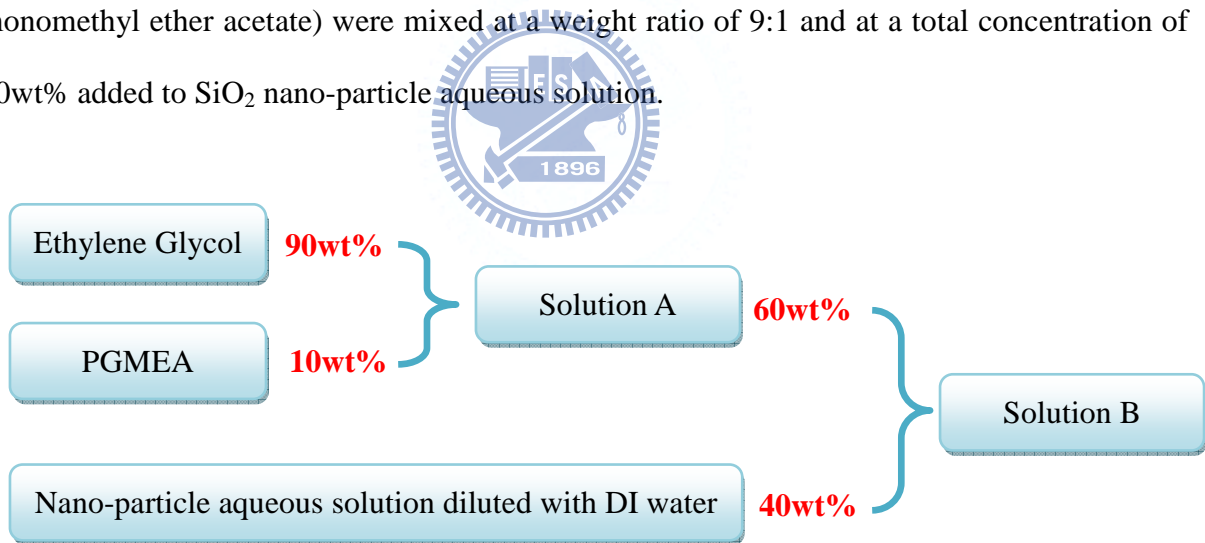


Fig. 4-1 The diagram of mixed method.

4.2 Cell Fabrication Process



Fig. 4-2 The flowchart of cell fabrication process.

- I. About experimental processes, the glasses used in this work were all pre-coated by Indium-Tin-Oxides (ITO) to make the glasses conducted. After cutting the ITO-coated glasses into small pieces of glasses that have $2\text{cm} \times 2.5\text{cm}$ areas, 5wt% detergent solution were used to clean the glass's surfaces. Each piece of glass was rinsed with detergent and rubbed by hands carefully. Then, the glass was washed with DI water until the water flowing along the surface smoothly. After that, the glass was loaded with a holder into DI water and shaken with ultra sonic for 20 minutes. Then, we refilled it with clean DI water and shook it with ultra sonic for 20 minutes again. The surface of glass was blew with nitrogen gas, and then baked for 30 minutes at 110°C . The surface was treated by UV-Ozone for 20 minutes in order to have better hydrophilic and adhesive.

II. In this step, different fabrication processes of mixture solution were shown below.

A. Nano-particle in DI water

The DI water was dropped on ITO glass to cover the whole glass for 60 seconds, and spun. It was for wetter surface and better adhesion of nano-particles solutions. Next, the diluted silicon oxides nano-particles aqueous solutions were dropped on the glass for 60 seconds and spun. The procedure of spin-coating is as **Table 4-1**.

Table 4-1 Parameters of spin coating nanoparticle.		
	Speed(rpm)	Time(sec)
Water-1 st spin	500	10
Water-2 nd spin	5000	60
Nanoparticle mixture solution-Waiting	0	60
Nanoparticle mixture solution -1 st spin	500	10
Nanoparticle mixture solution -2 nd spin	5000	60

After spin-coating, the samples were baked for 30 minutes at 110°C.

B. Nano-particle in PVA solution

The spin-coating parameter was changed as **Table 4-2**.

Table 4-2 Parameters of spin coating mixture solution.		
	Speed(rpm)	Time(sec)
Nanoparticle mixture solution-Waiting	0	60
Nanoparticle mixture solution -1 st spin	500	10
Nanoparticle mixture solution -2 nd spin	1200	30

After spin-coating mixture solution, the samples were baked for one hour at 110°C without spin-coating polyimide alignment layer. From the rubbing process to final process were the same as the general procedure.

C. Nano-particle in EG and PGMEA mixed solution

The procedure of spin-coating is as **Table 4-3**.

Table 4-3 Parameters of spin coating mixture solution.		
	Speed(rpm)	Time(sec)
Water-1 st spin	500	10
Water-2 nd spin	5000	30
Nanoparticle mixture solution-Waiting	0	30
Nanoparticle mixture solution -1 st spin	500	10
Nanoparticle mixture solution -2 nd spin	1500	30

After spin-coating mixture solution, the samples were baked for thirty minutes at 250°C .

- III. A solution consisted of polyimide (PI, Chisso PIA-X201-G01) and solvent were made. The ratio of the mixture solution will be PI: Solvent equals 1:1. The solution were filled into a glass syringe and put on a 0.2um filter to leach extra particles. The pure solvent and the mixture solution were used to spin first and second. The parameters of the spin coating are given as **Table 4-4**.

Table 4-4 Parameters of spin coating polyimide.		
	Speed(rpm)	Time(sec)
Solvent-Waiting	0	30
Solvent-1 st spin	800	30
Solvent-2 nd spin	5000	60
Polyimide mixture solution-Waiting	0	30
Polyimide mixture solution -1 st spin	800	30
Polyimide mixture solution -2 nd spin	5000	60

After this, the samples were baked for one hour at 220°C.

- IV. The sample glasses were rubbed by rubbing machine with the following parameters (**Table 4-5**).



Table 4-5 Rubbing Conditions for Polyimide glasses.	
Pile impression	0.2mm
Rotation speed	500rpm
Advancing speed	7.3mm/s

- V. UV glue, which is NOA-65 from Norland, mixed with about 5wt% spacer. We dropped a small amount of the mixture at four corner of the bottom plate. Then, the top plate was covered on top of it and pressed uniformly. The rubbing direction of top and bottom glasses was parallel. The cell was placed under a UV lamp to cure the glue for 5 minutes, and an empty cell was done.

VI. The cell gap of an empty cell was measured by UV/Vis spectrophotometer Lambda 650 (from Perkin Elmer). It was explained completely in section 3.3.

VII. The nematic liquid crystal, ZCE-5096XX (from Chisso), was injected into the cell by capillarity. The specification of ZCE-5096XX is shown in **Table 4-6**. We soldered the wire at the ITO contact, and then the test cell was completely done.

Table 4-6 The specification of liquid crystal material ZCE-5096XX.		
Sample	ZCE-5096XXXX	
$T_{N \rightarrow C[S]}$	<-20 °C	
$T_{N \rightarrow I}$	95.5 °C	
Viscosity η (at 20°C)	46.7 mPa · s	
Optical anisotropy (at 25°C 589nm)	Δn	0.158
	n_e	1.662
	n_o	1.504
Dielectric anisotropy (at 25°C)	$\Delta \epsilon$	10.0
	$\epsilon_{ }$	14.1
	ϵ_{\perp}	4.1
Specific resistivity ρ (at 25°C)	$>1.5 \cdot 10^{14} \Omega \cdot \text{cm}$	
K_{11}	9.8 dyne	
K_{22}	5.8 dyne	
K_{33}	11.8 dyne	
γ_1	178 mPas	

4.3 Optimum Nanostructure Surface

In order to uniform nano-particle distribution, we tried three methods to achieve optimum condition. The details of three methods were shown in this section.

4.3.1 Nano-particle in DI water

The nano-particles modified surface was prepared before polyimide layer. Silicon oxide (SiO_2) nano-particle aqueous solution (90 nm, mean diameter) was diluted with de-ionic (DI) water and coated on the substrate, as show in Fig. 4-3.

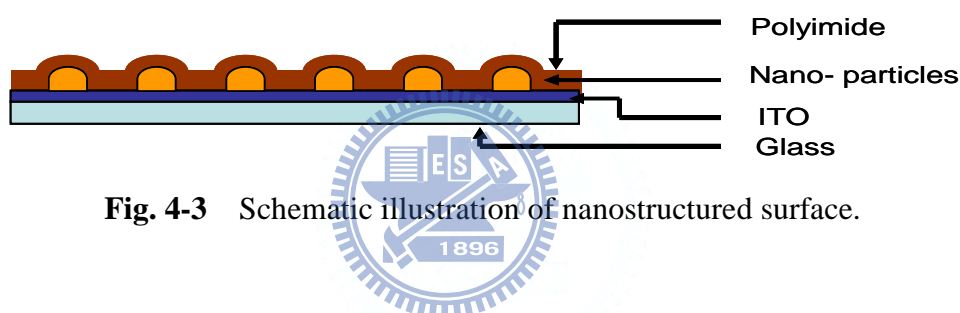


Fig. 4-3 Schematic illustration of nanostructured surface.

Fig. 4-4 shows the atomic force microscopy (AFM) images of different concentration, some aggregation of silicon oxide particles was found when the concentration was higher than 0.2 wt%. The relationship between nano-particle concentration and the distribution density was shown in Fig. 4-5. The average distribution density increased with increasing the nano-particle concentration.

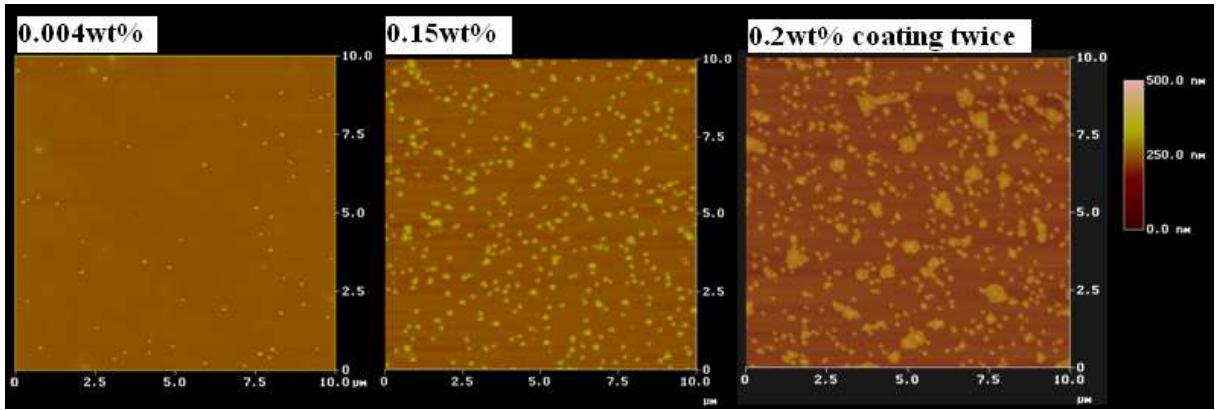


Fig. 4-4 The AFM images of different concentration.

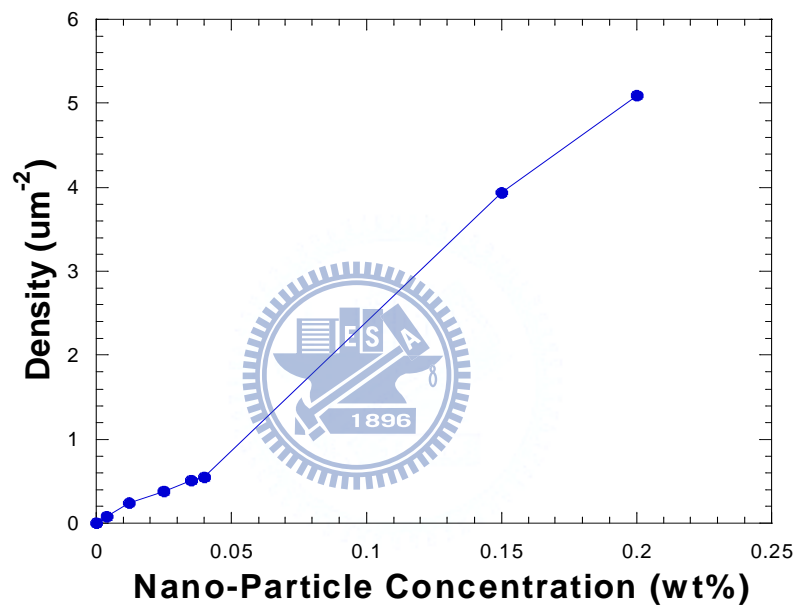


Fig. 4-5 The relation between concentration (wt%) and distribution density (μm^{-2}).

In this method, the limitation of increasing nano-particle distribution density with spin-coating fabrication technique was found. By spin-coating nano-particle twice can achieve higher distribution density. However, the aggregation and nonuniform nano-particle distribution around the center and edge of ITO surface, we called coffee ring effect, were observed by AFM images.

4.3.2 Nano-particle in PVA Solution

In order to increase the nano-particle density and get uniform distribution, considering increasing the viscosity of nano-particle solution. The silicon oxide nano-particle aqueous solution (90 nm, mean diameter) was diluted in DI water and mixed with PVA and Alcohol. The mixture solution was coated on the substrate, as shown in Fig. 4-6.

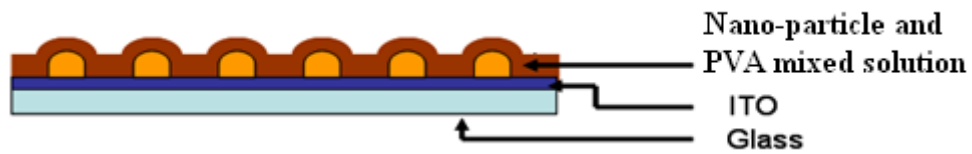
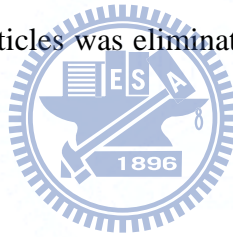


Fig. 4-6 Schematic illustration of nanostructured surface.

Fig. 4-7 shows the AFM images of different nano-particle concentration, the aggregation problem of silicon oxide nano-particles was eliminated obviously even the concentration was higher than 0.2 wt%.



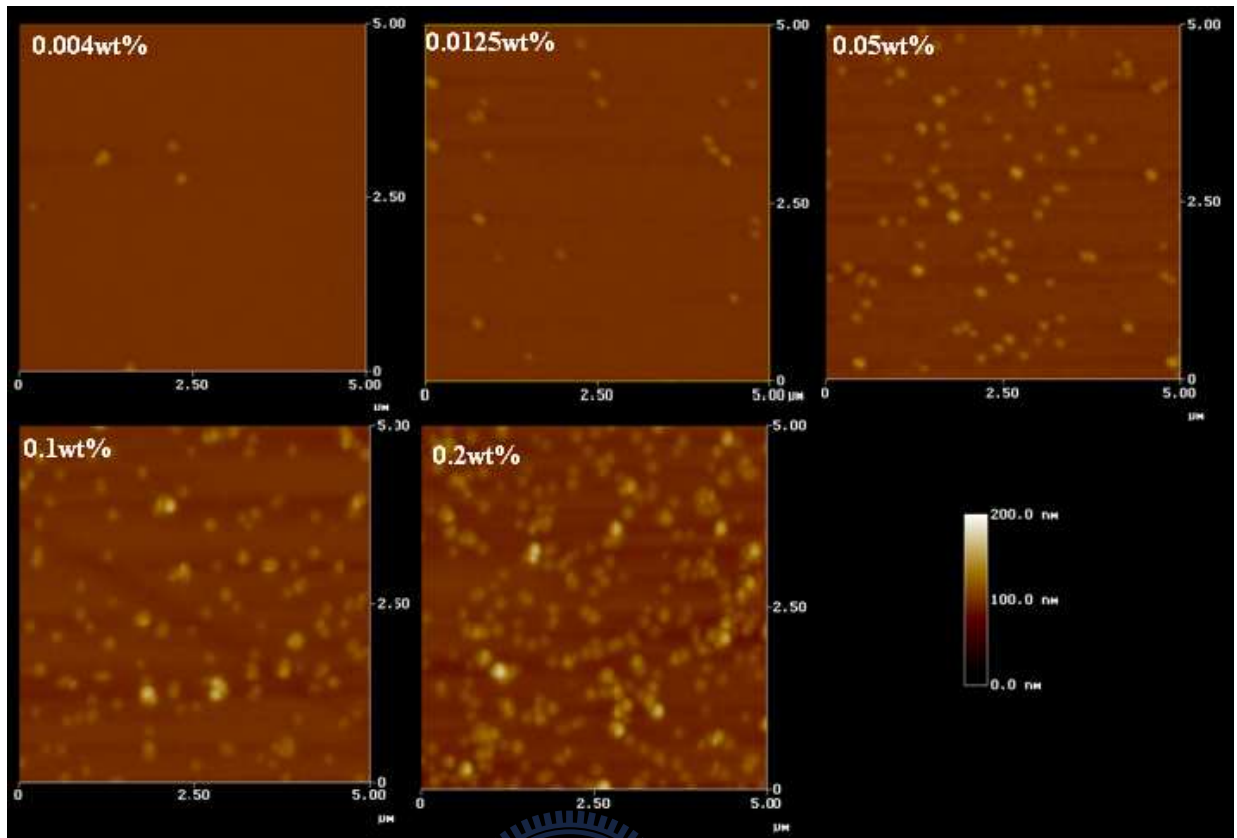


Fig. 4-7 The AFM images of different concentration.

The relationship between concentration and the distribution density was shown in Fig. 4-8. Fig. 4-8 shows that nano-particle concentration had a linear dependent with distribution density. Compared Fig.4-5 and Fig.4-8, the distribution density in PVA mixture solution is almost twice in water solution under the same nano-particle concentration. Moreover, the uniform distribution was observed by AFM images.

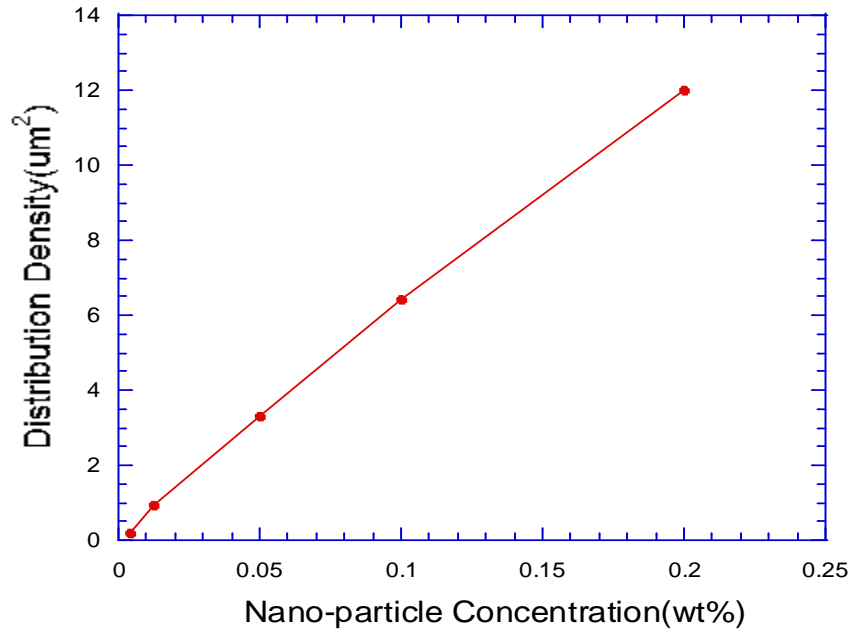


Fig. 4-8 The relation between concentration (wt%) and distribution density (μm^{-2}).

Although this method can solve the issues of coffee ring effect and aggregation, it still had the problem when measuring electro-optical properties to the test cell, which needed a longer Ha-to-bend transition time compared with the conventional OCB cell, as shown in **Table 4-7**. The original characteristics of OCB cells were destroyed. As a result, PVA material is not a suitable alignment layer of OCB cell.

Table 4-7 Comparison of transition time with PVA and PI alignment.

Nano-particle Concentration (wt%)	Distribution density (μm^{-2})	Cell gap (μm)	0V~6V(sec) Ha-to-bend	6V~0V(sec) twist-to-splay
Conventional OCB cell-PI	0	2.8	58	107
Conventional OCB cell-PVA	0	3.2	101	33
0.0125-PVA	0.92	3.18	83	23
0.1-PVA	6.4	3.16	62	11

4.3.3 Nano-particle in EG and PGMEA Mixed Solution

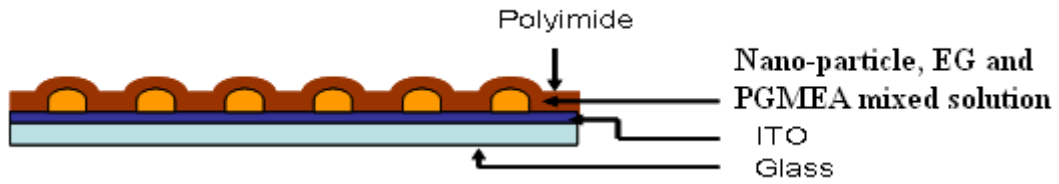
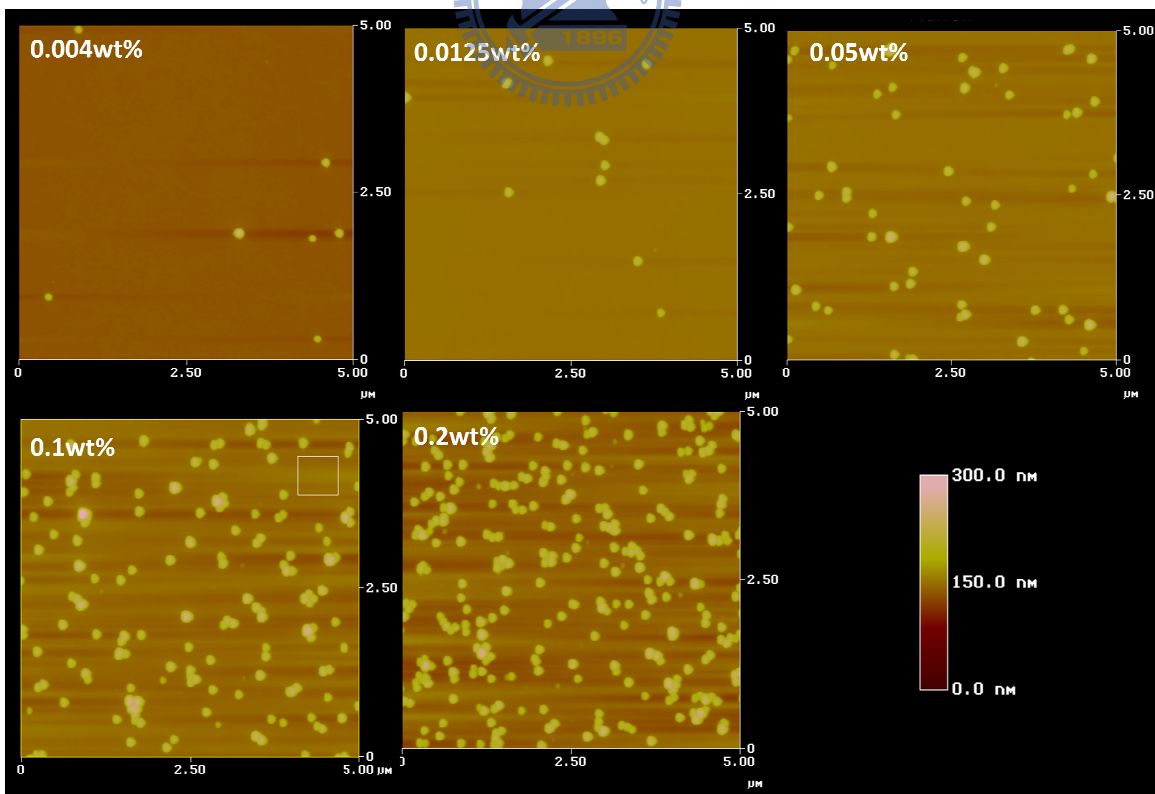


Fig. 4-9 Schematic illustration of nanostructured surface.

In order to solve the problem in PVA solution and keep the advantage of uniform distribution, we tried another mixture solution. The mixture solution was coated on the substrate, as shown in Fig. 4-9. In this method, two diameters of SiO₂ nano-particle, 50nm and 90nm, were used here. Fig. 4-10 and Fig. 4-11 show the AFM images of different concentration around the center and the edge of ITO surface. The uniform distribution of nano-particle on the ITO surface was observed here.



(a)

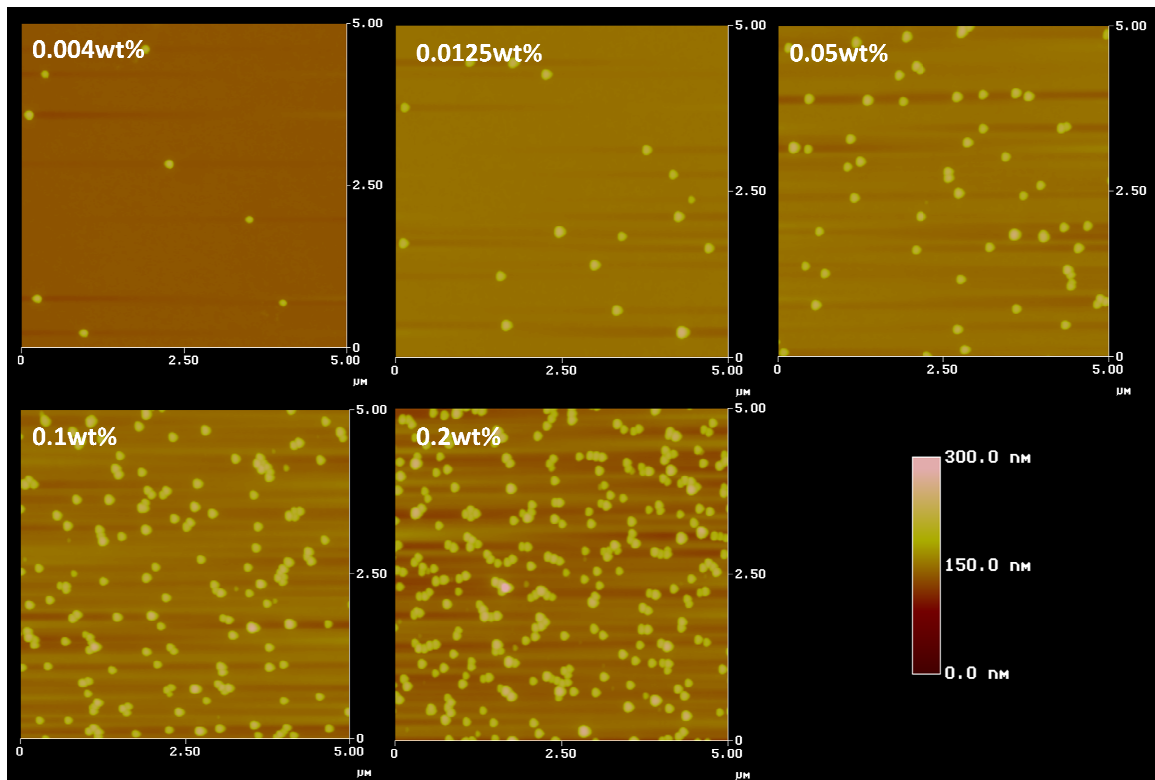
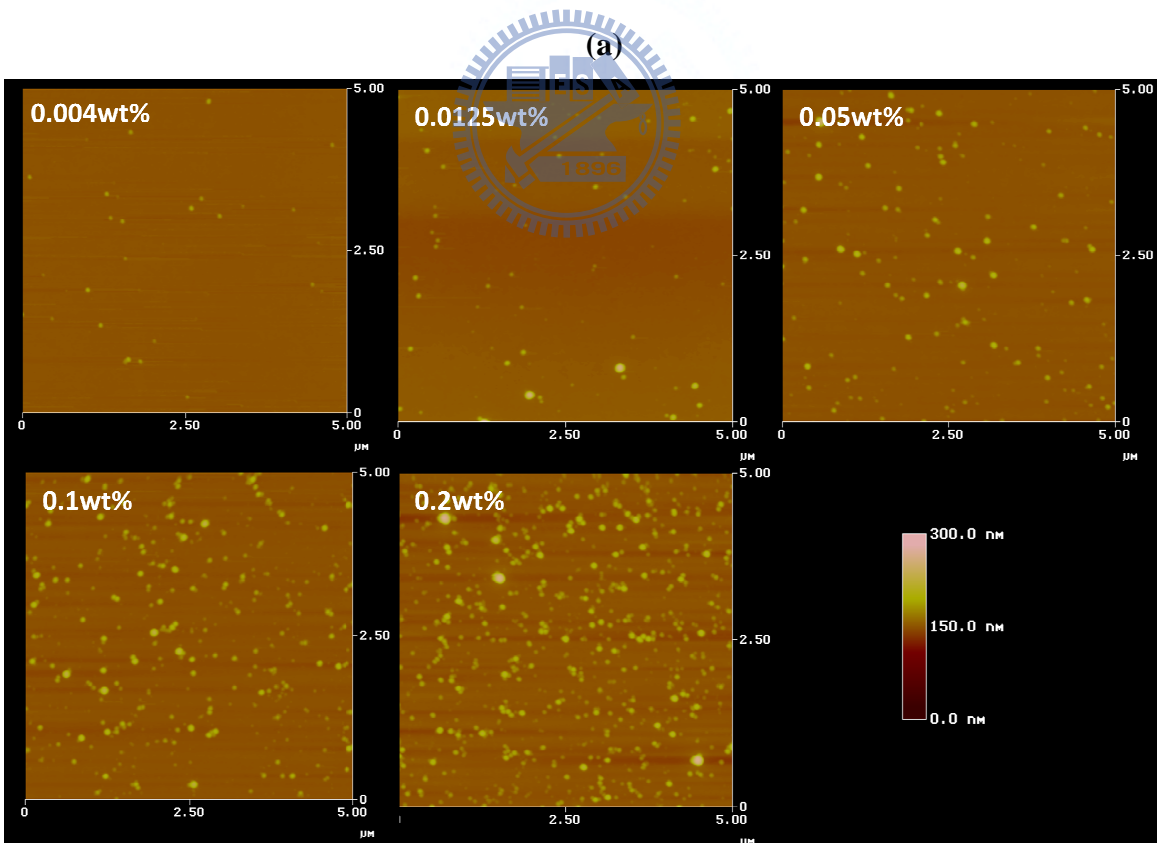
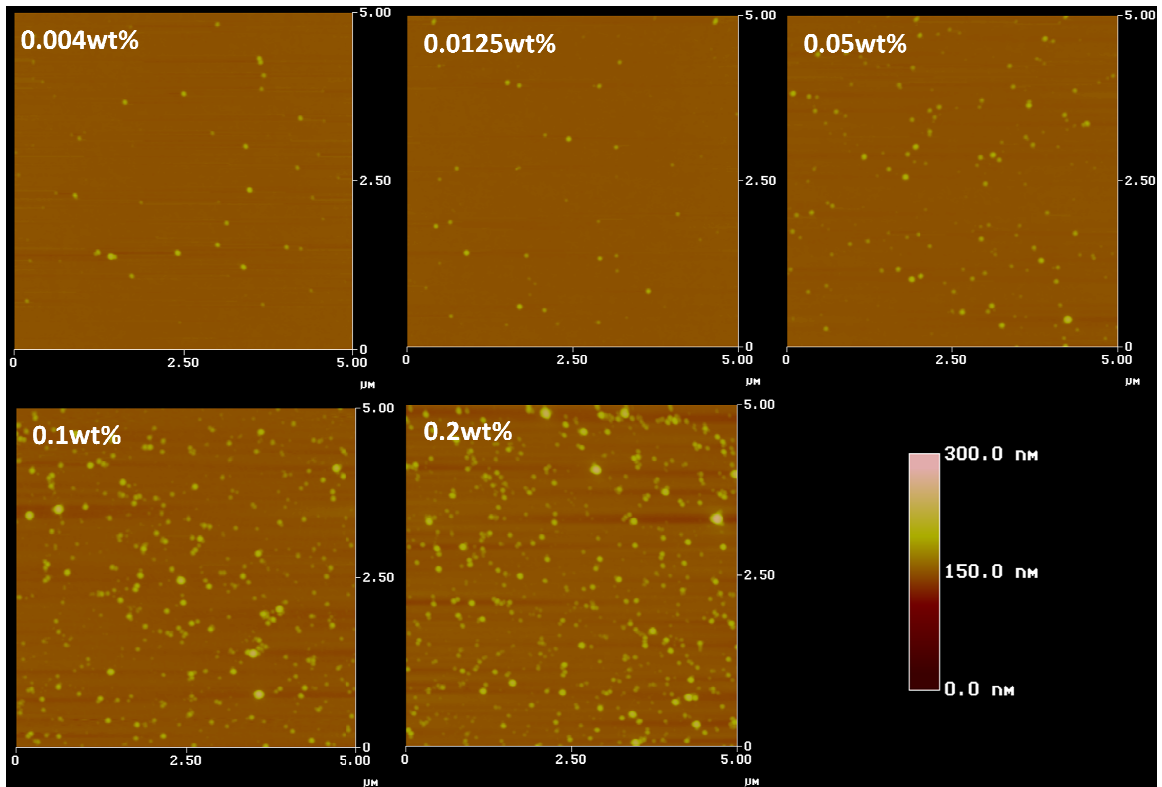


Fig. 4-10 The AFM images of 90nm nano-particle treated surface at different concentration.

(a) Around the center of ITO surface. (b) Around the edge of ITO surface.



(b)

Fig. 4-11 The AFM images of 50nm nano-particle treated surface at different concentration.

(a) Around the center of ITO surface. (b) Around the edge of ITO surface.

The AFM images of the nanostructure surface in this method were polyimide on top. The protrusions diameter of the surface treated with 90 nm nano-particle was in the region of 200-300nm, with the height of 80-150nm. The protrusions diameter and height were nonuniform on the surface treated with 50 nm nano-particle. Consequently, we separated the protrusion size to three kinds. First kind, the diameter was in the region of 200-300nm, with the height of 80-100nm. Second kind, the diameter was in the region of 150-200nm, with the height of 50-80nm. Third kind, the diameter was in the region of 100-150nm, with the height of 30-50nm.

A specific metric was proposed to unify the densities of different nano-particle sizes. We defined a standard volume which was in the $5\mu\text{m} \times 5\mu\text{m}$ area with the height of 103.5nm. The protrusion rate, the percentage of total protrusion volume in standard volume, in different nano-particle concentration was calculated. Fig.4-12 shows the relation between concentration (wt%) and protrusion rate (%) with 50nm and 90nm diameters nano-particle. The result shows that the relation between concentration (wt%) and protrusion rate (%) was almost linear dependent.

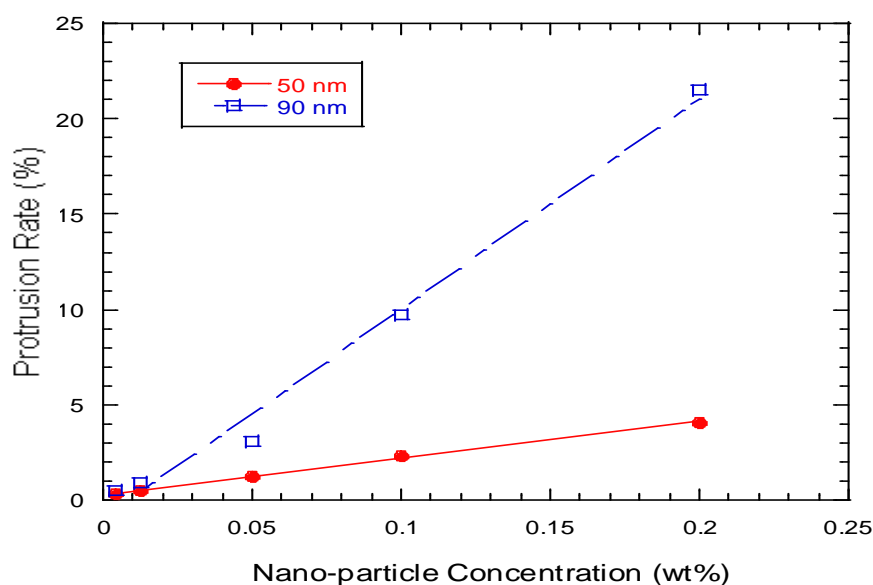


Fig. 4-12 The relation between concentration (wt%) and protrusion rate (%).

4.3.4 Summary



After trying three kinds of mixture solution, the EG and PGMEA mixed nano-particle solution not only can solve coffee ring effect but also can increase nano-particle density without serious aggregation. Furthermore, it still can keep the electro-optical characteristics of conventional OCB cell. As a result, in the following sections, many electro-optical characteristics will be measured and discussed by this technique.

4.4 Transition Time Measurement

Fig. 4-13 shows the picture of nucleation process of conventional OCB cell and nanostructure treated cell ($2.5 \times 2 \text{ cm}^2$, cell gap = $4.8 \text{ }\mu\text{m}$). The transition time was counted by the video image captured by video camera while applying AC square wave (6V). The frame rate was 25 fps (frames per second). The time of complete transition was counted in the film. It could be observed that the transition appeared in circles around the transition cores. The

Ultra Slim Lightbox (from Microlight Computer Co., Ltd.) which had two CCFL tubes as the light sources was used to be the backlight.

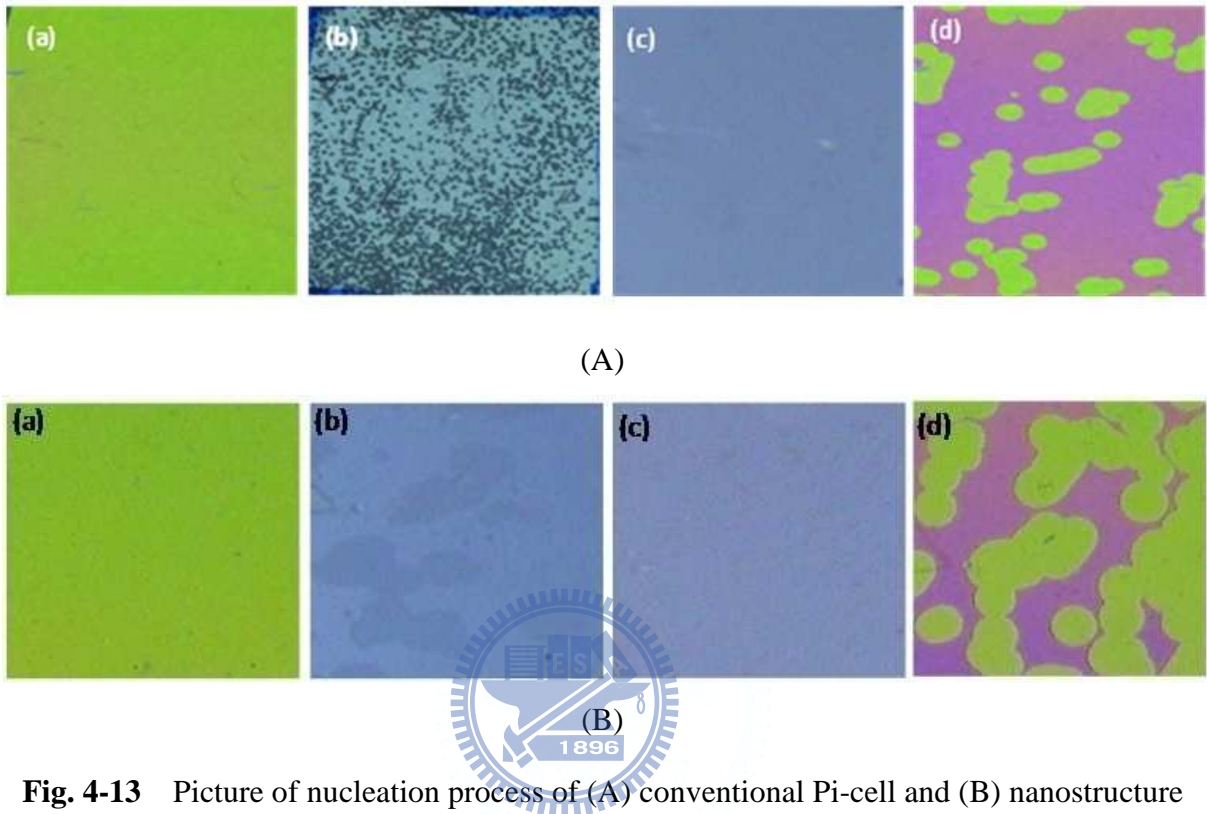


Fig. 4-13 Picture of nucleation process of (A) conventional Pi-cell and (B) nanostructure treated cell. The (a)(b)(c)(d) are the splay state, Ha to bend state, bend state, and twist to splay state, respectively.

The elapsed time from Ha-to-bend state and twist-to-splay state were calculated and summarized in the table below. [Table 4-8](#) and [Table 4-9](#) show the data of 90nm nano-particle treated test cell with cell gap around $4.67\mu\text{m}$ and $2.8\mu\text{m}$, respectively.

In $4.67\mu\text{m}$ cells, the transition time of splay-to-bend and the twist-to-splay were improved from 141 and 228sec to almost invisible, when the protrusion rate was over 3%. The transition time was also related with the cell gap, therefore the transition time of $2.8\mu\text{m}$ cells were faster than the $4.67\mu\text{m}$ cells. We also measured the transition time with applying

voltage from 0V to 3V in order to observe Ha-to-bend transition significantly.

Table 4-8 The transition time during nucleation for 90nm nano-particle (cell gap~4.67 μ m).

Nano-particle Concentration (wt%)	Protrusion rate (%)	0V~3V(sec)	0V~6V(sec) Ha-to-bend	6V~0V(sec) twist-to-splay	Response time(ms)
Conventional OCB cell	0	1078	141	228	3.43
0.004	0.47	905	127	121	3.42
0.0125	0.88	620	110	95.62	3.72
0.05	3.09	526	99(30%)	42(82%)	3.51
0.1	9.75	230	Invisible	2.1	13.22
0.2	21.50	131	Invisible	Invisible	12.61

Table 4-9 The transition time during nucleation for 90nm nano-particle (cell gap~2.8 μ m).

Nano-particle Concentration (wt%)	Protrusion rate (%)	0V~2.5V(sec)	0V~6V(sec) Ha-to-bend	6V~0V(sec) twist-to-splay	Response time(ms)
Conventional OCB cell	0	624	58.42	104.18	1.77
0.004	0.47	500	47.04	47.28	1.50
0.0125	0.88	430	43.93	30.28	1.53
0.05	3.09	118	Invisible (99.9%)	Invisible (99.9%)	1.25
0.1	9.75	60	Invisible	Invisible	6.53
0.2	21.50	58	Invisible	Invisible	6.64

Table 4-10 and Table 4-11 show the data of 50nm nano-particle treated cell with cell gap around 4.67 μ m and 2.8 μ m, respectively. The acceleration of Ha-to-bend transition time was determined obviously while applying voltage from 0V to 2.5V.

Table 4-10 The transition time during nucleation for 50 nm nano-particle (cell gap~4.67 μ m).

Nano-particle Concentration (wt%)	Protrusion rate (%)	0V~3V(sec)	0V~6V(sec) Ha-to-bend	6V~0V(sec) twist-to-splay	Response time(ms)
Conventional OCB cell	0	1078	141	228	3.43
0.004	0.35	1035	117	190	3.20
0.0125	0.49	790	66	123	3.25
0.05	1.24	745	28(80%)	96(58%)	2.98
0.1	2.30	718	2	10	13.80
0.2	4.11	670	Invisible	Invisible	14.00

Table 4-11 The transition time during nucleation for 50 nm nano-particle (cell gap~2.8 μ m).

Nano-particle Concentration (wt%)	Protrusion rate (%)	0V~2.5V(sec)	0V~6V(sec) Ha-to-bend	6V~0V(sec) twist-to-splay	Response time(ms)
Conventional OCB cell	0	624	58	104	1.77
0.004	0.35	517	30	68	1.30
0.0125	0.49	500	22	58	1.50
0.05	1.24	476	2(97%)	6(94%)	1.20
0.1	2.30	463	Invisible	Invisible	5.30
0.2	4.11	420	Invisible	Invisible	5.40

In summary, the higher the protrusion rate was, the less the splay-to-bend and twist-to-splay transition time were. However, the response time became slower from ~3 to ~13ms and ~1.5 to ~6ms with respect to 4.67 μ m and 2.8 μ m cells, when nano-particle concentration was over 0.05wt%. In other words, the nano-particle concentration was limited by cell response time. In section 4.6, the relationship between protrusion rate and transition time will be discussed.

4.5 Measurement of Electro-Optical Properties

Fig. 4-14 shows the V-T curves of 90nm and 50nm nano-particle treated cell with cell gap around 4.67 μ m and 2.8 μ m. The results show that the critical voltage and optical characteristics compared with conventional OCB cell were unchanged regardless of the

variation of nano-particle concentration. Most important, the nanostructures would not influence the transmittance of the device.

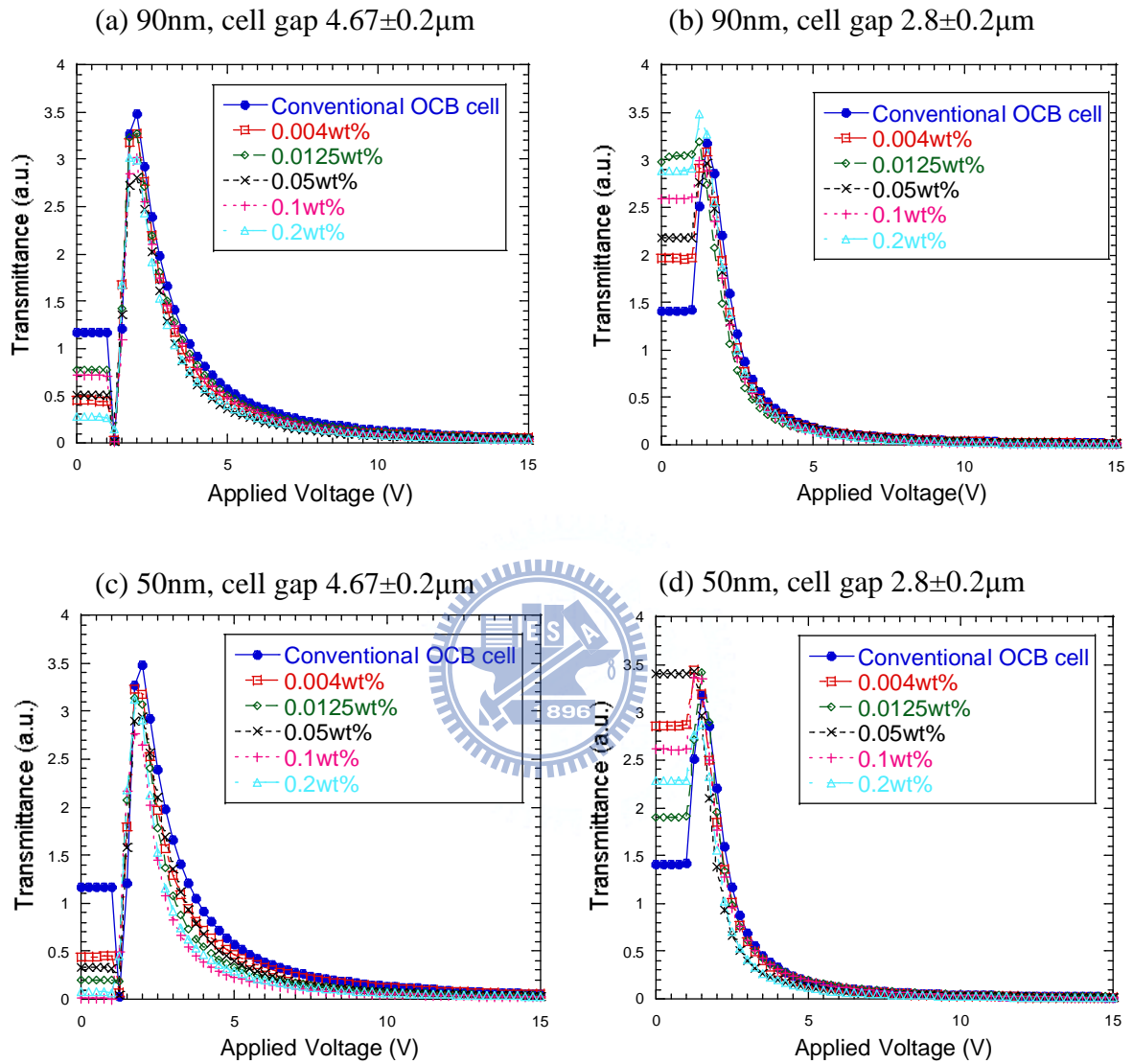
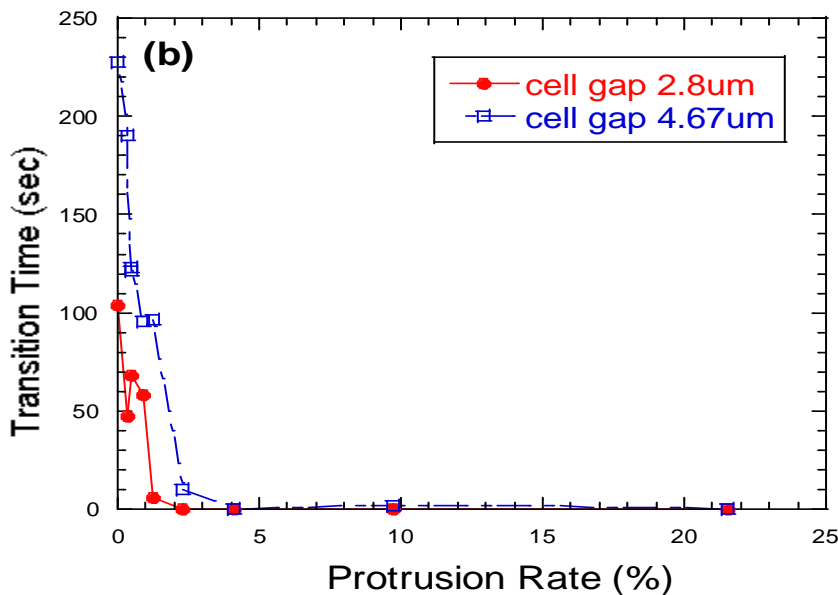
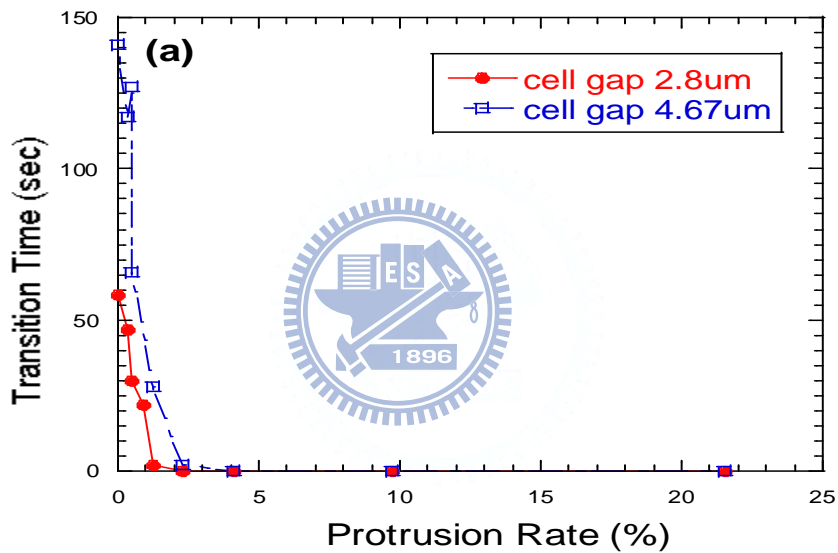


Fig. 4-14 The V-T curves in difference nano-particle concentration.

4.6 Discussion

The trend of transition time regarding to the protrusion rate was shown in **Fig. 4-15**. It shows that the higher the protrusion rate was, the less the Ha-to-bend and twist-to-splay transition time were. **Fig. 4-15(a)** and **Fig. 4-15(b)** described the Ha-to-bend and

twist-to-splay transition time respectively with cell gap around $2.8\mu\text{m}$ and $4.67\mu\text{m}$. The result indicated that the transition time rapidly decreased when the protrusion rate was over 3%. The transition time was also related with the cell gap; as a result, the transition time is much faster in the $2.8\mu\text{m}$ cell than the $4.67\mu\text{m}$ cell. In **Fig. 4-15(c)**, when applying voltage was near to critical voltage, 3V and 2.5V for cell gap around $4.67\mu\text{m}$ and $2.8\mu\text{m}$ respectively, we can observe this phenomenon obviously. The fitting curves of transition time were calculated by exponential functions (correlation coefficients R^2 were above 90%), which were matched with the theory mentioned before.



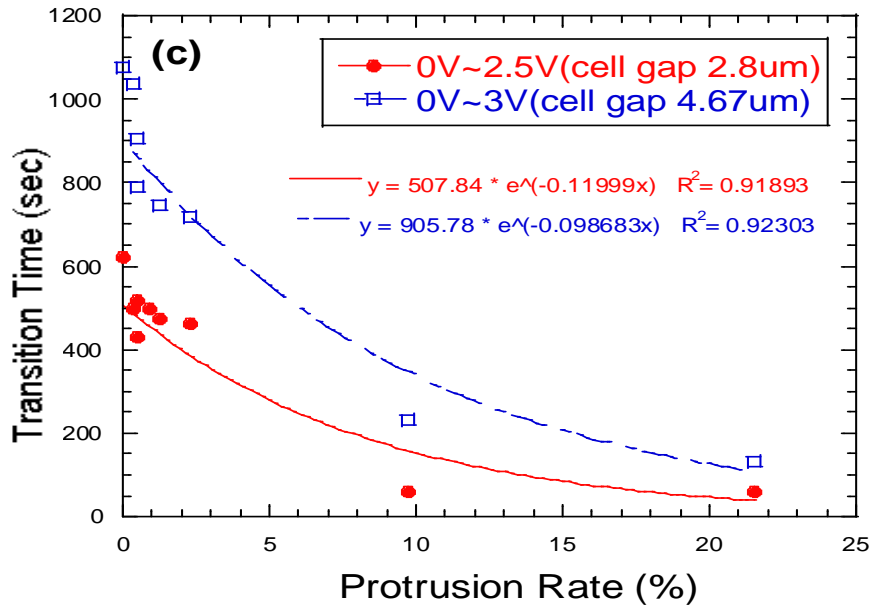
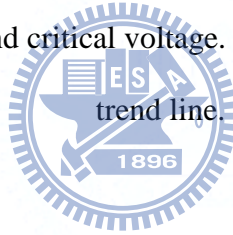


Fig. 4-15 The trend of transition time (sec) regarding to the protrusion rate (%) with cell gap around 2.8 μm and 4.67 μm . (a) Applied voltage from 0V to 6V. (b) Applied voltage from 6V to 0V. (c) Applied voltage around critical voltage. The solid line indicates the exponential



trend line.

We knew that surface inhomogeneity which makes strong strain energy in the local liquid crystal director field. [49] Considering the experiment results into nucleation theory, the strain energy was increased by nanostructure. The higher protrusion rate caused stronger strain energy. Consequently, from eq. 2-1, the change in free energy as a function can modify into:

$$\Delta G = \frac{4}{3} \pi r^3 (G_V + \Delta\delta) + 4\pi r^2 \sigma_{\alpha\gamma} \quad (\text{eq. 4-1})$$

Where $\Delta\delta$ is the energy gain from surface inhomogeneity. $\Delta\delta$ has a positive dependent to protrusion rate. G_V and $\Delta\delta$ are negative quantity, as a result, the energy barrier ΔG would diminish when $\Delta\delta$ increased. In summary, the higher protrusion rate can facilitate nucleation process.

Considering the nucleation rate, from eq. 2-5, we knew that the nucleation rate, I , depends on the average number of critical clusters and the diffusion of molecules to the cluster, β .

$$I = N \exp\left(\frac{-\Delta G^*}{k_B T}\right) \beta \quad (\text{eq. 4-2})$$

Where :

ΔG^* : critical free energy needed

N : the number of potential nucleation sites per unit volume

k_B : the Boltzmann constant

N is positive dependent to protrusion rate. From eq. 4-1, the critical free energy ΔG^* is diminished by nanostructure. The smaller ΔG^* and the larger N are, the larger transition rate is. The transition time is inversely proportioned to nucleation rate. As a result, we figure out that

$$\text{protrusion rate} \propto N \propto I \propto \frac{1}{\Delta t}$$

Where Δt indicates the transition time. Above all, the higher protrusion rate would lead to faster transition time.

4.7 Summary

In this study, a nucleation technique for obtaining fast transition to bend state in OCB cells without applying high pulse voltage has been achieved. We investigated the random distribution of silicon oxide nano-particles for decreasing the time of splay-to-bend transition in OCB cells. The nanostructure protrusions, which consist of silicon oxides nano-particles, became the bend transition core during nucleation. From the experimental results, the

transition speed had a positive relationship with protrusion rate. The transition time of splay-to-bend state and twist-to-splay had 99.9% reduction with protrusion rate over 3%. The limitation of the nano-particle concentration was clarified. At 0.05wt% nano-particle concentration, had a better performance for nanostructure treated cell.



Chapter 5

Conclusions

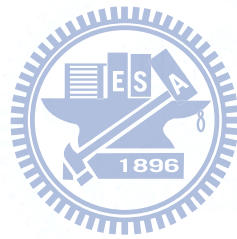
5.1 Conclusions

In this study, the fast transition from splay state to bend state in OCB cells has been achieved by nucleation technique. The protrusions, which consist of silicon oxides nano-particles, became the transition cores during nucleation. The optimum condition of nanostructure surface for OCB cells was presented here. The relationship between transition time and protrusion rate was investigated in this thesis. Moreover, the limitation of the nano-particle volume distribution density was clarified. This technique demonstrated a 99.9% reduction of transition time without high pulse voltage ($<6V$). Furthermore, the nanostructures would not influence the transmittance of the device. The electro-optical properties of nano-particle modified OCB cell were remained as well when nano-particle concentration under 0.05wt%.

5.2 Future work

The nanostructure successfully induced fast and uniform transition in OCB cells without reducing the transmittance of the devices. However, the response time was increased with increasing the nano-particle concentration. There exist an optimum concentration between 0.05wt% and 0.1wt% which would not only have fast response time but also reduce the transition time to almost invisible. In this thesis, we also tried to simplify the fabrication

process by mixing the nano-particle into PVA. Nevertheless, PVA is not a suitable alignment layer for OCB cells. If there is a new nano-particle material which can mix with polyimide uniformly, the fabrication process would be simplified.



References

- [1] F. Reinizer, *Monatsh. Chem.*, 9, 421 (1888)
- [2] O. Lehmann, *Z. Physik. Chem.*, 4, 462 (1889)
- [3] P. J. Bos, J. A. Rahma, and J. W. Doane, *Society for Info. Disp. Symp. Digest Tech.*, 24, 887 (1993)
- [4] Y. Tanaka, Y. Taniguchi, T. Sasaki, A. Takeda, Y. Koibe, and K. Okamoto, *Society for Info. Disp. Symp. Digest*, 206 (1999)
- [5] K. Iizuka, *Elements of Photonics, Volume I: In Free Space and Special Media*, (Wiley-Interscience, New York, 2002)
- [6] P. J. Bos, K.R. Koehler/Beran, *Mol. Cryst. Liq. Cryst.*, Vol. 113, 329 (1984)
- [7] Y. Yamaguchi, T. Miyashita, T. Uchida, *SID*, San Jose, USA, February, 19-04, p. 277 (1993)
- [8] C. L. Kuo, T. Miyashita, M. Suzuki, and T. Uchida, *Society for Info. Disp. Symp. Digest*, 927 (1994)
- [9] C. L. Kuo, T. Miyashita, M. Suzuki, and T. Uchida, *Jpn. J. Appl. Phys.*, part 2, 34, L1362 (1995)
- [10] T. Miyashita, and T. Uchida, *IEICE TRANS. Electron*, NO.8 August, E79-C, 1076 (1996)
- [11] H. G. Walton and M. J. Towler, *Liq. Cryst.*, 27, 1329 (2000)
- [12] S. T. Wu and A. M. Lackner, *Appl. Phys. Lett.*, 64, 2047 (1994)
- [13] Y. Yamaguchi, T. Miyashita, T. Uchida, *SID*, 19-04, p. 277 (1993)
- [14] E. J. Acosta, M. J. Towler and H. G. Walton, *Liq. Cryst.*, Vol. 27, p. 977 (2000).
- [15] P. D. Brimicombe and E. P. Raynes, *Liq. Cryst.*, Vol. 32, p. 1273 (2005).
- [16] P. D. Brimicombe and E. P. Raynes, *Appl. Phys. Lett.*, Vol. 89, p. 031121 (2006).
- [17] N. Nagae, T. Miyashita, T. Uchida, Y. Yamada, and Y. Ishii, *SID'00 Digest*, p.26 (2000)
- [18] F. S. Y. Yeung, and H. S. Kwok, *Appl. Phys. Lett.*, 88, 063505, (2006)
- [19] I. Inoue, T. Miyashita, T. Uchida, Y. Yamada, and Y. Ishii, *Eurodisplay*, p.179 (2002)
- [20] E. Acosta, B. Henley, D. Kean, M. Tillin, C. Tombling, M. Towler, E. Walton, H. Walton, and R. Winlow, *Liq. Cryst.*, Vol. 31, p.1619 (2004)
- [21] C. G. Jhun, J. L. Lee, S. H. Kang, S. L. Lee, J. C. Kim, T. H. Yoon, J. D. Noh, D. H. Suh, and J. Y. Lee, *IDW*, p.117 (2004)
- [22] K. Nakao, D. Suzuki, T. Kojima, M. Tsukane, and H. Wakemoto, *SID'04 Digest*, p.1416

(2004)

- [23] H. Kikuchi, H. Yamamoto, H. Sato, M. Kawakita, K. Takizawa, and H. Fujikake, *Jpn. J. Appl. Phys.*, Vol. 44, p.981 (2005)
- [24] S. H. Kim, and L. C. Chine, *Jpn. J. Appl. Phys.*, Vol. 43, p.7643 (2004)
- [25] F. F. Abraham, *Homogeneous nucleation theory*, (Academic Press, NY ,1974)
- [26] <http://en.wikipedia.org/wiki/Nucleation>
- [27] F. S. Ham, *J. Appl. Phys.*, Vol. 30, p.1518 (1959)
- [28] N. Nagae, T. Miyashita, T. Uchida, Y. Yamada and Y. Ishii, *SID*, p.26 (2000)
- [29] H. Nakamura and M. Noguchi, *Jpn. J. Appl. Phys.*, Vol. 39, P. 6368 (2000)
- [30] Y. Zhang, B. Wang, D. B. Chung, J. Colegrove and P. J. Bos, *SID*, 62.5L, p. 1782 (2005)
- [31] J. Cheng and R. N. Thurston, *J. Appl. Phys.*, Vol. 52(4), p. 2766 (1981)
- [32] I. Inoue, T. Miyashita, T. Uchida, Y. Yamada and Y. Ishii, *EuroDisplay*, p. 10-2 (2002)
- [33] F. Ogasawara, K. Kuboki, K. Wako, T. Uchida and A. yoshizawa, *Jpn. J. Appl. Phys.*, Vol. 48, p. L1148 (2009).
- [34] T. Satake and T. Kurata, *ASID Dig.*, p. 12-6 (2004)
- [35] T. Uchida, Y. Kimura, S. Kuniaki, H. Nakamura and Y. Taira, patent JP 9 185 037 (1995)
- [36] C. Lee, H. Chang, J. Lyu, K. Kim and J. Souk, *SID Dig.*, p-93. (2002)
- [37] N. Koma, T. Miyashita, K. Yoneda and T. Uchida, *SID*, p. 5.2 (1999)
- [38] M. Xu, D.-K. Yang, P. J. Bos, X. Jin, F. W. Harris and S. Z. D. Cheng, *SID*, 11.4L, p. 139 (1998)
- [39] X.-D. Mi, M. Xu, D.-K. Yang and P. J. Bos, *SID*, 5.1, p. 24 (1999)
- [40] F. S. Yeung, Y. W. Li and H.-S. Kwok, *Appl. Phys. Lett.*, Vol. 88, p. 041108 (2006)
- [41] F. S.-Y. Yeung, F.-C. Xie, H.-S. Kwok, J. Wau, O. Tsui, and P. Sheng, *SID*, 23.2, p.1080 (2005)
- [42] F. S.-Y. Yeung and H.-S. Kwok, *Appl. Phys. Lett.*, Vol. 88, p. 063505 (2006)
- [43] S.H. Lee, T.J. Kim, G.D. Lee, T.H. Yoon and J.C. Kim, *Jpn. J. Appl. Phys.*, Vol. 42, p. L1148 (2001).
- [44] E. Acosta, B. Henley, D. Kean, M. Tillin, C. Tombling, M. Towler, E. Walton, H. Walton and R. Winlow, *Liq. Cryst.*, Vol. 31, p.1619 (2004)
- [45] C.G. Jhun, J. L. Lee, S. H. Kang, S. L. Lee, J. C. Kim, T.-H. Yoon, J. D. Noh, D. H. Suh and J. Y. Lee, *IDW, LCTp1-5*, p. 117 (2004)
- [46] H. Kikuchi, H. Yamamoto, H. Sato, M. Kawakita, K. Takizawa and H. Fujikake, *Jpn. J. Appl. Phys.*, Vol. 44, p. 981 (2005)

[47]T. J. Chen, Y. H. Cheng and S. M. Wu, *Appl. Phys. Lett.*, Vol. 93, p. 221103 (2008)

[48]F. Bruyneel, H. D. Smet, J. Vanfleteren and A. V. Calster, *Opt. Eng.*, Vol. 40(2), p. 259
(2001)

[49]G. D. Lee, J. Anderson, and P. J. Bos, *Appl. Phys. Lett.*, Vol. 81, p. 03951(2002)

